The *Magnaporthe oryzae* MAX effector AVR-Pia binds a novel group of rice HMA domain-containing proteins

Josephine H.R. Maidment[1,2]*, Svenja C. Saile[1]*, Aurélien Bocquet[2], Céline Thivolle[1], Léo Bourcet[2], Lisa-Fatimatou Planel[1], Muriel Gelin[2], Thomas Kroj[1], André Padilla[2], Karine de Guillen[2]**, Stella Cesari[1]**

[1] PHIM Plant Health Institute, Univ Montpellier, INRAE, CIRAD, Institut Agro, IRD, Montpellier, France.
[2] Centre de Biologie Structurale, INSERM, CNRS, Université de Montpellier, 29 rue de Navacelles, 34090, Montpellier, France

*Contributed equally
**Corresponding authors

Stella Cesari
Tel: +33 4 99 62 48 62
Email: stella.cesari@inrae.fr

Karine de Guillen
Tel: +33 4 67 41 77 08
Email: karine.deguillen@cbs.cnrs.fr

ORCID
Josephine H.R. Maidment: 0000-0002-8229-2718
Svenja C. Saile: 0000-0003-2258-3166
Aurélien Bocquet: 0009-0007-0082-6098
Céline Thivolle: 0009-0000-5048-3619
Léo Bourcet: 0009-0004-4568-3543
Lisa-Fatimatou Planel: 0009-0007-5159-7109
Muriel Gelin 0000-0003-1320-8663
Thomas Kroj: 0000-0002-3752-1788
André Padilla: 0000-0001-9702-4612
Karine de Guillen: 0000-0002-5037-2115
Stella Cesari: 0000-0001-8558-0371

Keywords: pathogen effector, host virulence targets, rice blast fungus, rice, protein structure, plant defence, heavy metal associated domain, MAX effector

Abstract

Phytopathogenic fungi secrete effector proteins to promote virulence. MAX (*Magnaporthe* Avrs and ToxB-like) effectors form a sequence-diverse family sharing a conserved protein structure. AVR-Pia, a MAX effector from the rice blast fungus *Magnaporthe oryzae,* is recognised by the paired rice nucleotide-binding leucine-rich repeat immune receptors OsRGA4/OsRGA5 through direct binding to an integrated heavy metal-associated (HMA) domain in OsRGA5. Here, we identify previously unknown host targets of AVR-Pia: four HMA domain-containing rice proteins, belonging to the HMA Isoprenylated Plant Protein (HIPP) and HMA Plant Protein (HPP) families. AVR-Pia interacts with all four proteins both in vitro and in planta and binds their HMA domains with varying affinities. The crystal structure of AVR-Pia bound to the HMA domain of OsHPP09 revealed the molecular details of the binding interface. Structure-guided mutagenesis of OsHPP09 identified a single point mutation which prevents AVR-Pia binding, providing a foundation for targeted engineering of HMA domains to evade effector binding.

52 ## Introduction

53 The fungal pathogen *Magnaporthe oryzae* (syn. *Pyricularia oryzae*) is the causative agent of
54 rice blast, one of the most devastating diseases affecting cultivated rice worldwide [1,2]. Beyond
55 rice, this pathogen also causes severe yield losses in other cereals, including millets, barley
56 and wheat, and poses a threat to global food security [3].

57 To successfully colonize host plants, *M. oryzae* has evolved mechanisms to evade plant
58 defense responses and manipulate host cellular pathways to its advantage. A key element of
59 its pathogenic strategy is the secretion of a large collection of effector proteins. A subset of
60 these belong to the *Magnaporthe* AVRs and ToxB-like (MAX) effector family which has
61 undergone massive expansion in *M. oryzae* [4]. A characteristic feature of MAX effectors is their
62 conserved structural fold consisting of two β-sheets, each composed of three antiparallel β-
63 strands, stabilised by one or more disulphide bonds. Despite this structural conservation, MAX
64 effectors lack sequence similarity, resulting in differences in surface properties. Some
65 members also carry variable N- and C-terminal extensions, which may enable them to target
66 a broad range of host proteins [5–7].

67 AVR-Pia is a MAX effector present in approximately 20% of the *M. oryzae* isolates that infect
68 rice. It is highly expressed during the biotrophic phase of host colonization and contributes to
69 fungal virulence on rice [4,6,8]. In certain rice varieties, AVR-Pia is directly recognised by the
70 intracellular immune receptor OsRGA5, a nucleotide-binding leucine-rich repeat (NLR) protein
71 that functions together with the helper NLR OsRGA4 to activate immune responses and
72 restrict the spread of *M. oryzae* isolates expressing AVR-Pia [9–11]. Canonical plant NLRs
73 consist of an N-terminal signaling domain, a central nucleotide-binding domain and a C-
74 terminal leucine-rich repeat domain [12]. However, many NLRs also carry non-canonical
75 integrated domains (IDs), which are thought to originate from host proteins targeted by
76 pathogen effectors [13]. These IDs, found across diverse plant species, are believed to function
77 as mimics or baits for effector recognition ("integrated decoy" model) [13–16]. Both AVR-Pia and
78 a second MAX effector, AVR1-CO39, bind to the HMA ID of OsRGA5, despite sharing limited
79 sequence similarity [9,10]. This suggests that these effectors may target host proteins containing
80 HMA domains as part of their virulence strategy. However, to date, no host targets of AVR-
81 Pia or AVR1-CO39 have been identified, and their specific virulence functions remain
82 unknown.

83 Sequence analyses have shown that the OsRGA5-HMA domain shares sequence similarity
84 with the HMA domains of two related families of HMA domain-containing proteins [17]: HMA

85 domain-containing Plant Proteins (HPPs) and HMA domain-containing Isoprenylated Plant
86 Proteins (HIPPs). These two families are collectively referred to hereafter as H(I)PPs. H(I)PPs
87 are small metallochaperone-like proteins characterized by the presence of one or two HMA
88 domains, each adopting an α/β sandwich structure with a βαββαβ topology. Typically, the HMA
89 domain features a metal-binding MxCxxC motif, implicating H(I)PPs in roles related to metal
90 homeostasis [18,19]. However, approximately a third of rice H(I)PPs possess degenerate
91 MxCxxC motifs, suggesting functional diversification beyond metal binding.

92 Unlike HPPs, HIPPs carry a C-terminal CaaX motif that undergoes isoprenylation [20,21], a post-
93 translational modification involving the covalent attachment of an isoprenoid lipid to the
94 cysteine residue in the motif. This modification promotes membrane association of proteins [22].
95 Additionally, many HIPPs harbour proline-rich regions between the HMA domain and the
96 CaaX motif, which may be important in mediating protein-protein interactions [20,23].

97 Notably, H(I)PPs have undergone extensive expansion in vascular plants, with approximately
98 100 members identified in rice [17,20,24,25]. Most remain functionally uncharacterized, although
99 several have been implicated in response to various biotic and abiotic stresses [20,26–28].
100 Increasing evidence points to a broader role of H(I)PPs as susceptibility factors in interactions
101 with pathogens, pests, and viruses [17,29–39].

102 In cereals, H(I)PPs have been identified as susceptibility factors for *M. oryzae* infection [17,31,32].
103 Notably, some of these H(I)PPs are targeted by the MAX effectors AVR-Pik and APikL2[17,40,41]
104 AVR-Pik specifically interacts with members of a defined phylogenetic subclade (referred to
105 as clade A) of OsH(I)PPs, including among others OsHIPP19, OsHIPP20, OsHPP03, and
106 OsHPP04 [17,41]. OsHIPP20 has been functionally validated as a susceptibility gene, as its loss-
107 of-function mutation results in reduced sensitivity to *M. oryzae* [17].

108 Similar to AVR-Pia and AVR1-CO39, recognition of AVR-Pik in rice involves direct binding of
109 the effector to an HMA ID in the NLR receptor OsPik-1, which operates together with another
110 NLR protein, OsPik-2, to confer resistance [42,43]. The HMA domain of OsPik-1 belongs to the
111 same phylogenetic clade as the H(I)PPs targeted by AVR-Pik, reinforcing the idea that effector
112 targets may serve as templates for domain integration into NLRs.

113 Structural analyses of complexes between the MAX effectors AVR-PikF or APikL2 and the
114 HMA domains of their respective H(I)PP targets have revealed a conserved binding interface
115 [40,41]. In both cases, crystal structures show that β3 of the MAX fold and β4 of the HMA domain
116 are aligned in an antiparallel orientation, resulting in the formation of a β-sheet comprising the
117 four β-strands of the HMA domain and β-strands 3, 4 and 5 of the MAX fold. The interface is

118 globally similar to that observed in the crystal structures of AVR-Pik and the HMA ID of OsPik-
119 1, although the interface between AVR-PikF and OsHIPP19-HMA extends across a larger
120 area and involves additional hydrogen bonds [41].

121 By contrast, the crystal structure of AVR1-CO39 bound to the HMA ID of OsRGA5 revealed a
122 markedly different interface. Here, β2 of the core MAX fold of AVR1-CO39 and β2 of OsRGA5-
123 HMA are aligned, resulting in a β-sheet comprising the four β-strands of the HMA domain, and
124 β2, β1 and β6 of the MAX fold [10]. NMR titration experiments were used to map the OsRGA5-
125 interacting surface of AVR-Pia, and the results, combined with structural modelling and
126 mutagenesis, indicated that both effectors bind to OsRGA5-HMA at a similar interface [10,11,44].
127 Additionally, a crystal structure of AVR-Pia in complex with the HMA ID of OsPikp-1 revealed
128 a comparable binding interface, indicating that AVR-Pia binds different HMA domains in a
129 structurally similar manner [45].

130 More recently, the crystal structure of the MAX effector Pwl2 bound to OsHIPP43 showed that,
131 similar to the interface between AVR1-CO39 and AVR-Pia with OsRGA5-HMA, β2 of the core
132 MAX fold of Pwl2 and β2 of OsHIPP43-HMA are aligned [46]. However, unlike AVR-Pia and
133 AVR1-CO39, in addition to its core MAX fold, Pwl2 has a C-terminal extension comprising an
134 α-helix and unstructured region. This extension contributes significantly to the HMA binding
135 interface [46].

136 Collectively, these structural studies underscore the remarkable diversity with which MAX
137 effectors have evolved to target various HMA domain-containing proteins. They support the
138 hypothesis that AVR-Pia and AVR1-CO39 may engage distinct H(I)PP targets, different from
139 those bound by other MAX effectors, through unique interfaces.

140 MAX effectors constitute the largest arsenal of molecular weapons in *M. oryzae*. Identifying
141 their virulence targets, particularly for effectors that contribute directly to pathogenicity such
142 as AVR-Pia, and elucidating the molecular and structural basis of these interactions is of
143 critical importance. This knowledge will be instrumental in revealing the mechanisms exploited
144 by *M. oryzae* during the early stages of host infection. Furthermore, the identification of new
145 H(I)PP targets of *M. oryzae* effectors may provide opportunities for engineering blast
146 resistance, and possibly resistance to other pathogens that exploit H(I)PPs as susceptibility
147 factors. Such strategies could include bioengineering approaches aimed at disrupting effector-
148 target interactions in crop species. Finally, uncovering the targets of AVR-Pia would also bring
149 valuable evolutionary insights into the origin of its recognition by the NLR-ID receptor
150 OsRGA5.

151 Here, we identified four OsH(I)PPs as specific interactors of AVR-Pia. Our analyses revealed
152 that none of them are bound by other MAX effectors, including AVR1-CO39, AVR-Pik and
153 Pwl2. This finding suggests that although these MAX effectors commonly bind to HMA
154 domains, they have evolved to recognise different host targets. Using biochemical and
155 biophysical approaches, we validated and further characterized the interaction between AVR-
156 Pia and one of the interactors, OsHPP09. The crystal structure of AVR-Pia/OsHPP09-HMA
157 complex revealed extensive intermolecular hydrogen bonding and shows overall structural
158 similarity to the AVR1-CO39/OsRGA5-HMA complex. Guided by the AVR-Pia/OsHPP09-HMA
159 crystal structure, we identified a point mutation in OsHPP09 which disrupts its interaction with
160 AVR-Pia without compromising the HMA fold.

161

162 # Results

163 **AVR-Pia interacts with rice H(I)PPs in Y2H screening**

164 As AVR-Pia is recognised by OsRGA5 through direct binding to its HMA ID [9,11], we
165 hypothesized that AVR-Pia may target HMA domain-containing proteins to promote host
166 susceptibility.

167 To identify potential H(I)PP host targets of AVR-Pia, we conducted extensive pairwise yeast
168 two-hybrid (Y2H) assays. We screened a signal peptide-deleted version of AVR-Pia (dSP-
169 AVR-Pia, 20 – 85 aa) fused to the Gal4 activation domain (AD) against a rice HMA domain
170 library [47] comprising 80 rice HMA domains fused to the Gal4 DNA binding domain (BD).
171 Through this analysis, we identified five HMA domains that interact with AVR-Pia: OsHPP09
172 (LOC_Os03g02070), OsHIPP41 (LOC_Os03g06080), OsHPP11 (LOC_Os04g45130),
173 OsHIPP14 (LOC_Os04g39320) and OsHIPP39 (LOC_Os03g02860) (**Fig. 1a,**
174 **Supplementary Fig. 1, Supplementary Table 1**). Among these, BD:OsHPP09 paired with
175 AD:AVR-Pia conferred strong yeast growth on interaction-selective media, indicating a robust
176 interaction. In contrast, the remaining candidates led to only weak yeast growth when co-
177 expressed with AD:AVR-Pia.

178 We additionally tested the rice HMA library against the well-characterized MAX effectors Pwl2
179 and AVR-PikD. Consistent with earlier publications, we observed dSP-Pwl2 (22 – 145 aa)
180 interacting with the HMA domain of OsHIPP43, and dSP-AVR-PikD (22 – 113 aa) interacting
181 with the HMA domains of OsHIPP19, OsHIPP20, and other phylogenetically related HMA
182 domains [17,32,41,46] (**Supplementary Fig. 1**), confirming the integrity and sensitivity of our
183 screen.

184 In addition to this targeted pairwise analysis, an independent Y2H screen using a rice cDNA
185 library identified another HMA domain-containing protein, OsHIPP21 (LOC_Os09g09830), as
186 a putative interactor of AVR-Pia (**Supplementary Table 1, Supplementary Table 2**).
187 Together, these findings suggest that AVR-Pia might target a specific set of OsH(I)PPs.

188 We next examined whether the corresponding full-length (FL) proteins of all identified putative
189 interactors also associate directly with AVR-Pia, and tested them along with their isolated HMA
190 domains in a pairwise Y2H assay. Interestingly, interaction between AVR-Pia and OsH(I)PP
191 FL proteins was retained for only a subset of proteins: OsHPP09, OsHPP11 and OsHIPP21
192 (**Fig. 1a and Supplementary Fig. 2**), even though immunoblot analyses confirmed the
193 expression of all tested proteins (**Supplementary Fig. 3a, 3b, 3c**). Given that FL HPPs and
194 HIPPs differ by the presence of a C-terminal isoprenylation motif in HIPPs, and since
195 isoprenylation is known to promote membrane association of proteins [22], we aimed to rule out

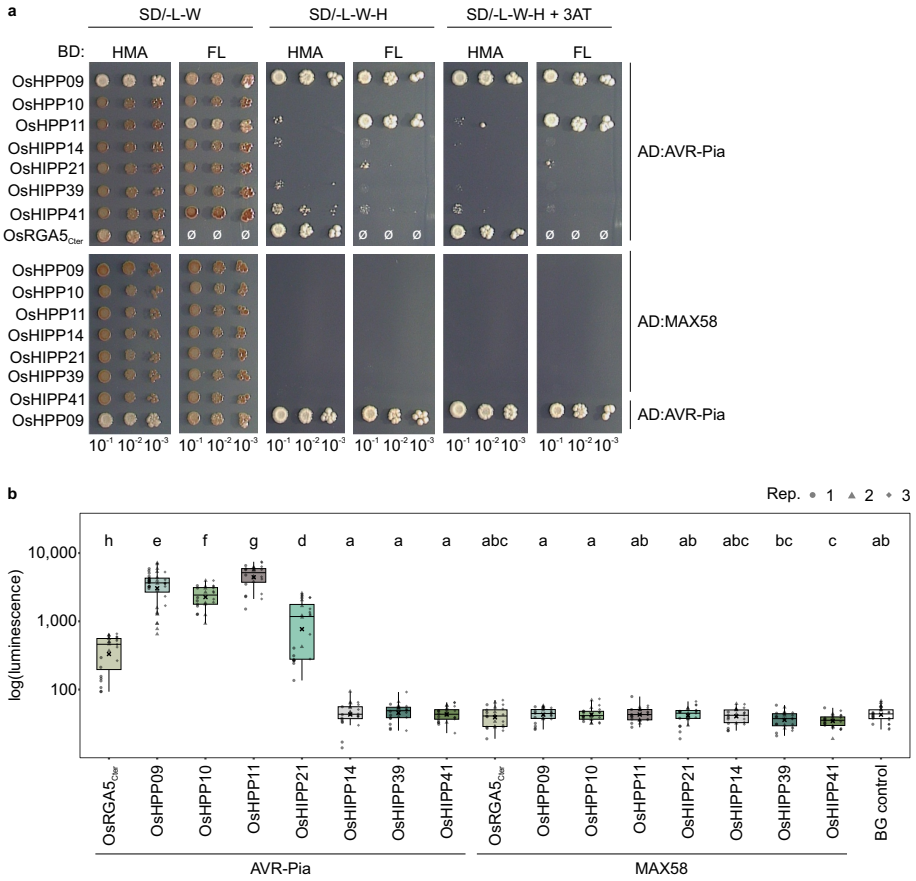

Fig. 1. AVR-Pia interacts with OsH(I)PPs.

a Y2H interaction analysis between AVR-Pia (upper panel) or MAX58 (lower panel) and either the heavy metal-associated (HMA) domain or full-length (FL) proteins of OsH(I)PPs. The OsH(I)PP candidates were previously identified in a comprehensive pairwise Y2H analysis using AVR-Pia as prey and a library of HMA domains from OsH(I)PPs as bait. $OsRGA5_{Cter}$ (883 – 1116 aa) was included as a positive control in the experiment with AVR-Pia/OsH(I)PPs (top panel). After an interaction was observed between OsHPP09 and AVR-Pia, this interaction was used as a positive control in the subsequent experiment with MAX58 (bottom panel).. Serial dilutions of diploid yeast were spotted onto synthetic defined (SD) media to monitor growth (SD/-LW) or to assess protein-protein interactions (SD/-LWH and SD/-LWH supplemented with 0.5 mM 3AT). Photos were taken after 7 days of incubation. Ø indicates positions where no yeast was spotted. AD, activating domain; BD, binding domain. **b** Quantitative measurement of luciferase-derived signals shows that AVR-Pia, but not MAX58, interacts with OsHPP09, OsHPP10, OsHPP11 and OsHIPP21 in a split-luciferase complementation assay. Neither AVR-Pia nor MAX58 interact with any other tested OsHIPP in planta. AVR-Pia and MAX58 were fused to the N-terminal part of luciferase (3xHA:NLuc:AVR-Pia, 3xHA:NLuc:MAX58) and co-expressed with OsH(I)PP FL proteins fused at their N-termini to the C-terminal part of luciferase (3xFlag:CLuc:OsH(I)PP). Co-expression of AVR-Pia with $OsRGA5_{Cter}$ (883 – 1116 aa) was used as a positive control. Leaves infiltrated with P19 alone served as background (BG) control. Leaf discs were collected 2 days post infiltration. Box plots show the median (line), mean (cross) and upper/lower quartiles (box limits), whiskers extend to the most extreme data points within 1.5x the interquartile range. Values outside this range are shown as individual data points. Three independent replicates were performed (n = 8 per replicate). Due to experimental constraints, the following sample sizes apply to specific conditions: AVR-Pia/OsHPP09: n = 16 in replicates 1 and 2. Data points are individually plotted and shaped according to the replicate. Different letters indicate statistically significant differences based on a pairwise Wilcoxon test (α = 0.05).

219 the possibility that the studied FL HIPPs might not localize efficiently to the yeast nucleus,
220 potentially causing false-negative results in Y2H assays. To test this, we generated mutant
221 versions of the respective FL HIPPs, replacing the cysteine residue within the isoprenylation
222 motif with a serine residue, thereby preventing isoprenylation (**Supplementary Fig. 3a, 3b**).
223 However, this mutation did not restore interactions of FL OsHIPPs (OsHIPP14, OsHIPP39,
224 OsHIPP41) with AVR-Pia in Y2H assays (**Supplementary Fig. 2**).

225 The HMA domains of OsHPP09 and OsHPP11 share high sequence similarity with OsHPP10
226 (LOC_Os10g36200) (91.5 % and 74.6 % identical, respectively; **Supplementary Fig. 4**).
227 Surprisingly, despite this high level of conservation, neither the HMA domain nor the FL
228 version of OsHPP10 interacted with AVR-Pia in Y2H assays (**Fig. 1a**). By contrast, OsHIPP21
229 shares only 30-40% sequence identity with the HMA domains of the three OsHPPs
230 (**Supplementary Fig. 4**). Similar to OsHPP10, the HMA domain of OsHIPP21 did not interact
231 with AVR-Pia. However, AVR-Pia interacted with FL OsHIPP21. Taken together, these results
232 suggest that AVR-Pia interacts with and potentially targets OsHPP09, OsHPP11, and
233 OsHIPP21 in rice.

234 A previous study classified MAX effectors into 20 groups based on structural features [5].
235 MAX58 belongs to the same group as AVR-Pia, but the two effectors differ in surface
236 properties [5]. dSP-MAX58 (20-86 aa) did not interact with any of the tested OsH(I)PPs (neither
237 their HMA domains nor the FL versions) in Y2H assays (**Fig. 1a, Supplementary Fig. 1**),
238 although the effector protein was expressed (**Supplementary Fig. 3c**). These findings
239 suggest that, despite their shared structural fold, effectors with distinct surface properties
240 target different host proteins.

241 **AVR-Pia interacts with rice H(I)PPs in planta**

242 To test whether AVR-Pia and the four OsH(I)PPs also interact in planta, we performed split-
243 luciferase complementation assays in *Nicotiana benthamiana*. 3xFlag-CLuc-OsH(I)PP FL
244 proteins were co-expressed with 3xHA-NLuc-dSP-AVR-Pia or 3xHA-NLuc-dSP-MAX58.
245 Luminescence was measured from leaf discs collected 2 days after infiltration. Co-expression
246 of FL OsHPP09, OsHPP11, and OsHIPP21 with AVR-Pia led to high luminescence levels,
247 exceeding even those observed for the positive control $OsRGA5_{Cter}$ (883 – 1116 aa), which
248 includes the HMA ID, in complex with AVR-Pia (**Fig. 1b**). Strikingly, we also detected a strong
249 luminescence signal for OsHPP10/AVR-Pia, although no interaction between OsHPP10 and
250 AVR-Pia was observed in Y2H assays (**Fig. 1b**). The luminescence level for OsHPP10/AVR-
251 Pia was slightly lower than those of OsHPP09 and OsHPP11 but within a similar range, and
252 exceeded that of OsHIPP21. Consistent with our Y2H results, no interaction was observed in
253 planta between AVR-Pia and other tested FL OsHIPPs, including OsHIPP14, OsHIPP39 and

254 OsHIPP41 (**Fig. 1b**). Additionally, MAX58 showed no detectable interaction with any of the
255 tested OsH(I)PPs in split-luciferase complementation experiments (**Fig. 1b**). Expression of all
256 proteins in *N. benthamiana* was confirmed by immunoblot analyses (**Supplementary Fig. 5**).
257 Collectively, these data demonstrate that AVR-Pia interacts with OsHPP09, OsHPP10,
258 OsHPP11 and OsHIPP21 in planta.

259 **AlphaFold Multimer models cannot differentiate between HMA domains which are**
260 **bound by AVR-Pia and those which are not**

261 Several studies have reported the use of AlphaFold Multimer to differentiate between pairs of
262 effectors/host proteins which interact and those which do not [17,48,49]. We therefore tested
263 whether structural models of AVR-Pia in complex with experimentally verified interactors
264 (OsHPP09-HMA, OsHPP10-HMA, OsHPP11-HMA and OsHIPP21-HMA) showed
265 differences, either in the models themselves or in the associated confidence metrics,
266 compared to structural models of AVR-Pia with non-interacting HMA domains. We modelled
267 AVR-Pia/HMA complexes using AlphaFold2 and AlphaFold3. High confidence models were
268 obtained for all AVR-Pia/HMA pairs except AVR-Pia/OsHIPP42-HMA using AlphaFold2
269 (**Supplementary Fig. 6**) and for all AVR-Pia/HMA pairs except AVR-Pia/OsHIPP41-HMA
270 using AlphaFold3 (**Supplementary Fig. 7**). For the AlphaFold2 models, interface analysis with
271 qtPISA revealed a tendency towards increased interface area for AVR-Pia-interacting HMA
272 domains compared to non-interacting HMA domains. (**Supplementary Fig. 6)**. By contrast,
273 interface analysis (qtPISA) did not indicate any significant differences in the interface area,
274 binding energy, or number of intermolecular contacts for AlphaFold3 models of AVR-Pia-
275 interacting HMA domains compared to non-interacting HMA domains (**Supplementary Fig.**
276 **7**). Overall, AlphaFold models do not show a clear differentiation between HMA domains which
277 are bound by AVR-Pia and those which are not.

278 **AVR-Pia-H3 does not interact with OsHPP09, OsHPP10, OsHPP11 and OsHIPP21**

279 Two non-synonymous polymorphisms in AVR-Pia (F24S and T46N) have emerged in a subset
280 of rice-infecting *M. oryzae* isolates, disrupting the interaction with OsRGA5 and thereby
281 enabling these isolates to evade recognition by rice varieties carrying the OsRGA4/OsRGA5
282 NLR pair [9,11] (**Supplementary Fig. 8**). This virulence-associated allele is referred to as AVR-
283 Pia-H3 [9]. We next investigated whether these polymorphisms also affect direct binding to the
284 putative host target H(I)PPs. Pairwise Y2H assays revealed that, unlike wild-type AVR-Pia,
285 the AVR-Pia-H3 variant failed to interact with the HMA domains and FL versions of OsHPP09,
286 OsHPP10, OsHPP11 and OsHIPP21 (**Fig. 2a**). Protein expression of AVR-Pia-H3 was
287 confirmed by immunoblot (**Supplementary Fig. 3c**).

288

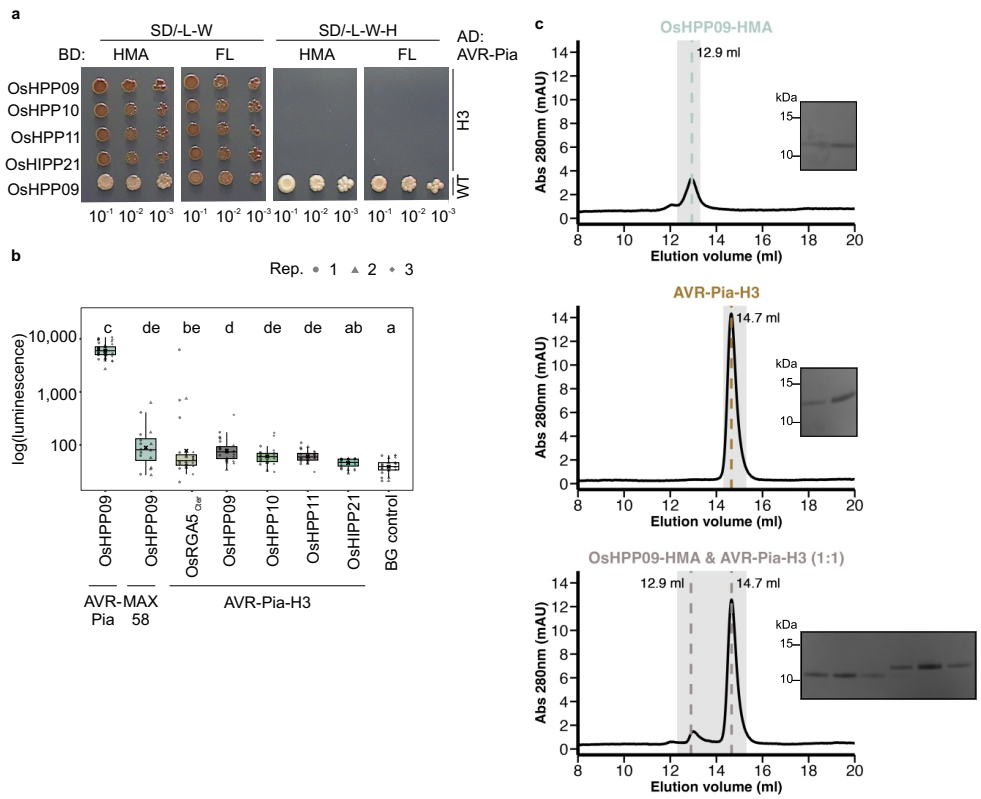

Fig. 2. AVR-Pia-H3 does not interact with OsHPP09, OsHPP10, OsHPP11 and HIPP21.

a Y2H interaction analysis between AVR-Pia-H3 and either the heavy metal-associated (HMA) domain or full-length (FL) proteins of OsH(I)PPs. OsHPP09/AVR-Pia served as positive control. Serial dilutions of diploid yeast were spotted onto synthetic defined (SD) media to monitor growth (SD/-LW) or to assess protein-protein interactions (SD/-LWH). Photos were taken after 7 days of incubation. AD, activating domain; BD, binding domain. **b** Quantitative measurement of luciferase-derived signals shows that AVR-Pia-H3 does not interact with OsHPP09, OsHPP10, OsHPP11 and OsHIPP21 in a split-luciferase complementation assay. MAX effectors were fused to the N-terminal part of luciferase (3xHA:NLuc:MAX) and co-expressed with OsH(I)PP FL proteins fused at their N-termini to the C-terminal part of luciferase (3xFlag:CLuc:OsH(I)PP). Co-expression of AVR-Pia with OsHPP09 served as positive control, co-expression of OsHPP09/MAX58 and $OsRGA5_{Cter}$ (883 – 1116 aa)/AVR-Pia-H3 served as negative controls. Leaves infiltrated with P19 alone served as background (BG) control. Leaf discs were collected 2 days post infiltration. Box plots show the median (line), mean (cross) and upper/lower quartiles (box limits), whiskers extend to the most extreme data points within 1.5x the interquartile range. Values outside this range are shown as individual data points. Three independent replicates were performed, with n = 8 per combination per replicate. Due to experimental constraints, the following sample sizes apply to specific conditions: AVR-Pia/OsHPP09: n = 16 in replicates 1 and 2. Data points are individually plotted and shaped according to the replicate. Different letters indicate statistically significant differences based on a pairwise Wilcoxon test ($\alpha = 0.05$). **c** Analytical gel filtration traces obtained from injection of OsHPP09-HMA alone (top panel), AVR-Pia-H3 alone (middle panel) and the two proteins in a 1:1 molar ratio (bottom panel). Significant peaks are indicated by coloured dashed lines with the elution volume labelled. SDS-PAGE gel inserts show fractions from peak elution volumes indicated by the grey shaded regions. OsHPP09-HMA absorbs light at 280 nm poorly (molar extinction coefficient of 1490 $M^{-1}cm^{-1}$) so the peak corresponding to OsHPP09-HMA is small. The elution volume observed for OsHPP09-HMA is consistent with dimerisation, as has been observed for other purified HMA domains [10,50]. There is no shift in the elution volume for AVR-Pia-H3 in the presence of OsHPP09-HMA indicating that the two proteins do not form a complex.

315 To validate these findings in planta, we performed split-luciferase complementation assays
316 following transient co-expression of OsH(I)PPs and AVR-Pia-H3 in *N. benthamiana*. Only
317 weak luminescence signals were detected for AVR-Pia-H3 with OsH(I)PPs, comparable to the
318 negative control pair $OsRGA5_{Cter}$/AVR-Pia-H3 and OsHPP09/MAX58, and markedly lower
319 than the positive control OsHPP09/AVR-Pia (**Fig. 2b**). These results suggest that the AVR-
320 Pia-H3 polymorphisms severely diminish effector-target binding. Protein expression was
321 confirmed by immunoblot analysis (**Supplementary Fig. 9**). We also tested for an interaction
322 between purified AVR-Pia-H3 and OsHPP09-HMA proteins in vitro using analytical size
323 exclusion chromatography. AVR-Pia-H3 had a peak elution volume of 14.7 ml when analysed
324 alone, while OsHPP09-HMA had a peak elution volume of 12.9 ml (consistent with
325 dimerisation, as has been reported for other HMA domains in solution) (**Fig. 2c**). The elution
326 volumes of the two proteins were unchanged when a 1:1 mixture of the proteins was analysed,
327 indicating that they did not form a stable complex in vitro (**Fig. 2c**). By contrast, the peak
328 elution volume of AVR-Pia shifted from 15.3 ml when analysed alone to 12.7 ml following
329 incubation with OsHPP09-HMA (1:1 effector:HMA ratio), consistent with the formation of an
330 AVR-Pia/OsHPP09-HMA complex (**Supplementary Fig. 10**).

331 Together, these data indicate that the same mutations that disrupt NLR recognition also
332 abolish the ability of AVR-Pia to bind to its candidate host targets, suggesting that AVR-Pia
333 might use a similar binding interface for interacting with both the host targets and the immune
334 receptor during recognition.

335 **AVR1-CO39 does not interact with OsHPP09, OsHPP10, OsHPP11 and OsHIPP21**

336 As the HMA ID of OsRGA5 also binds the MAX effector AVR1-CO39 [9,10] we tested whether
337 AVR-Pia and AVR1-CO39 bind to the same subset of H(I)PPs. To this end, we tested
338 interactions between dSP-AVR1-CO39 (22 – 89 aa) and the HMA domain as well as FL
339 version of OsHPP09, OsHPP10, OsHPP11 and OsHIPP21 in Y2H assays. AVR1-CO39 did
340 not interact with either the HMA domains or FL versions of any of these rice proteins, whereas
341 interaction with $OsRGA5_{Cter}$ including the HMA ID was confirmed (**Fig. 3a**). Effector
342 expression in yeast was confirmed by immunoblot analysis (**Supplementary Fig. 3c**).

343 To assess whether these interactions occur in planta, we performed split-luciferase
344 complementation assays in *N. benthamiana*. We observed only weak luminescence signals
345 indicating low-level interactions between AVR1-CO39 and FL OsHPP09, OsHPP10 and
346 OsHPP11. However, these signals were substantially lower than those observed for the AVR-
347 Pia/OsHPP09 interaction (**Fig. 3b**). Consistent with our Y2H results, no interaction was
348 detected between FL OsHIPP21 and AVR1-CO39, similar to the negative control combination
349 OsPi21/AVR1-CO39 (**Fig. 3b**). Protein expression was validated by immunoblot analysis

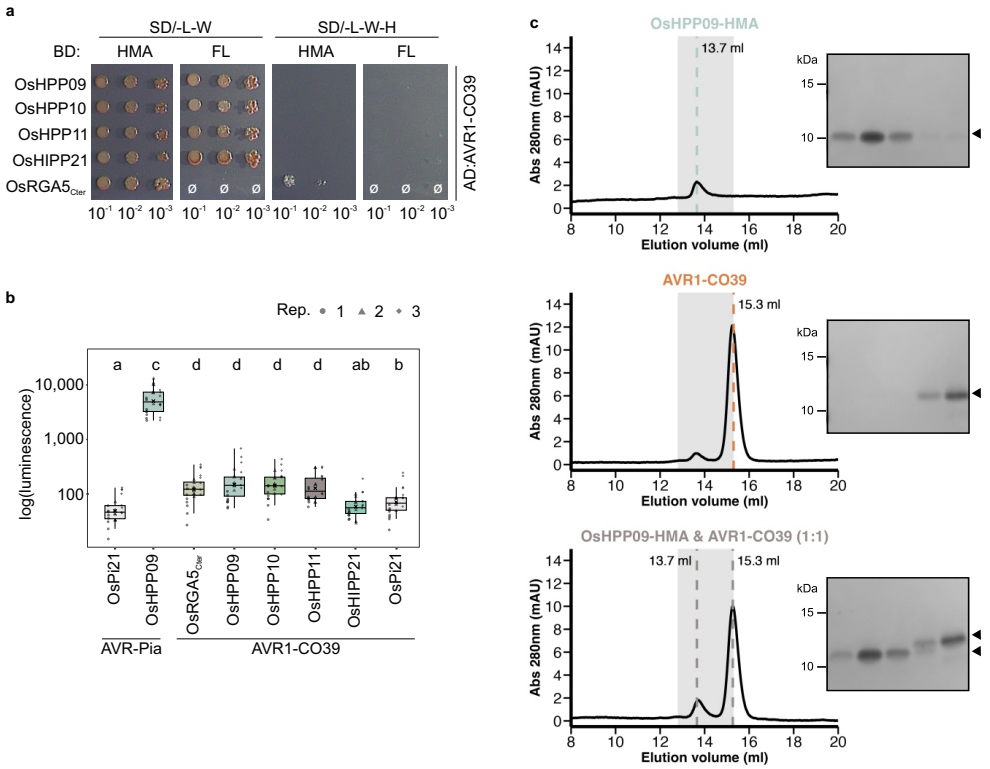

Fig. 3. OsH(I)PPs interacting with AVR-Pia do not interact with AVR1-CO39.

a Y2H interaction analysis between AVR1-CO39 and either the heavy metal-associated (HMA) domain or full-length (FL) proteins of OsH(I)PPs. $OsRGA5_{Cter}$ (883 – 1116 aa)/AVR1-CO39 served as positive control. Serial dilutions of diploid yeast were spotted onto synthetic defined (SD) media to monitor growth (SD/-LW) or to assess protein-protein interactions (SD/-LWH). Photos were taken after 7 days of incubation. Ø indicates positions where no yeast was spotted. AD, activating domain; BD, binding domain. **b** Quantitative measurement of luciferase-derived signals shows that AVR1-CO39 does weakly interact with OsHPP09, OsHPP10 and OsHPP11 but not with OsHIPP21 in a split-luciferase complementation assay. MAX effectors were fused to the N-terminal part of luciferase (3xHA:NLuc:MAX) and co-expressed with OsH(I)PP FL proteins fused at their N-termini to the C-terminal part of luciferase (3xFlag:CLuc:OsH(I)PP). Co-expression of AVR-Pia or AVR1-CO39 with OsPi21 served as negative controls, while AVR-Pia/OsHPP09 served as a positive control. Leaf discs were collected 2 days post infiltration. Box plots show the median (line), mean (cross) and upper/lower quartiles (box limits), whiskers extend to the most extreme data points within 1.5x the interquartile range. Values outside this range are shown as individual data points. Three independent replicates were performed, with n = 8 per combination per replicate. Data points are individually plotted and shaped according to the replicate. Different letters indicate statistically significant differences based on a pairwise Wilcoxon test ($\alpha = 0.05$). **c** Analytical gel filtration traces obtained from injection of OsHPP09-HMA alone (top panel), AVR1-CO39 alone (middle panel) and the two proteins in a 1:1 molar ratio (bottom panel). Significant peaks are indicated by coloured dashed lines with the elution volume labelled. SDS-PAGE gel inserts show fractions from peak elution volumes indicated by the grey shaded regions. OsHPP09-HMA absorbs light at 280 nm poorly (molar extinction coefficient of 1490 $M^{-1}cm^{-1}$) so the peak corresponding to OsHPP09-HMA is small. The small peak at ~13.7 ml in the trace for AVR1-CO39 is likely due to some dimerisation of the AVR1-CO39 protein; the quantity of protein is insufficient to observe a corresponding band on the SDS-PAGE gel. The elution volume observed for OsHPP09-HMA is consistent with

374 dimerisation, as has been observed for other purified HMA domains [10,50]. There is no shift in the elution volume
375 for AVR1-CO39 in the presence of OsHPP09-HMA indicating that the two proteins do not form a complex.
376

377 (**Supplementary Fig. 11**). Analytical size-exclusion chromatography with purified proteins
378 further supported the absence of complex formation (**Fig. 3c**).

379 Collectively, these results suggest that although AVR1-CO39 and AVR-Pia are both
380 recognised by the same HMA ID in OsRGA5, they do not target the same H(I)PPs in the host.

381 **AVR-Pia interacts with a distinct group of H(I)PPs to AVR-Pik and Pwl2**

382 Previous studies have shown that the MAX effectors AVR-PikC, AVR-PikD and Pwl2 target
383 H(I)PPs [17,32,41,46]. To investigate whether the OsH(I)PPs identified as AVR-Pia interactors
384 (OsHPP09, OsHPP10, OsHPP11 and OsHIPP21) also associate with AVR-Pik or Pwl2, we
385 tested their pairwise interactions using Y2H assays. Our results revealed that neither the HMA
386 domain nor the FL versions of these proteins bound directly to dSP-AVR-PikC (22 – 113 aa),
387 dSP-AVR-PikD (22 – 113 aa) or dSP-Pwl2 (22 – 145 aa) (**Fig. 4a**). As a control, we confirmed
388 the known interactions of AVR-PikC and AVR-PikD with OsHIPP19 and OsHIPP20, and Pwl2
389 with OsHIPP43 (**Fig. 4a**). Interestingly, we observed that AVR-Pia also directly interacted with
390 FL OsHIPP19 under low-stringency Y2H conditions (**Fig. 4a**).

391 The lack of interaction between AVR-PikC and AVR-PikD with the FL proteins OsHPP09,
392 OsHPP10, OsHPP11 and OsHIPP21 was further validated through split-luciferase
393 complementation assays using proteins transiently expressed in *N. benthamiana* (**Fig. 4b**).
394 AVR-Pia showed a strong interaction with OsHIPP19 and a weaker interaction with OsHIPP20
395 (**Fig. 4b**). Co-expression of Pwl2 with OsHPP09, OsHPP10, OsHPP11 and OsHIPP21
396 resulted in very weak luminescence. Protein expression was confirmed by immunoblot
397 analysis (**Supplementary. Fig. 12**).

398 Together, our findings indicate that the HMA domains bound by AVR-Pia are not targeted by
399 AVR-Pik and Pwl2. Despite sharing a conserved MAX effector fold, these effectors seem to
400 generally engage different target H(I)PPs, highlighting the specificity of effector-host target
401 interactions.

402 **AVR-Pia interacts with the HMA domains of OsHPP09, OsHPP10, OsHPP11 and**
403 **OsHIPP21 with varying affinities**

404 To determine the affinity with which AVR-Pia binds to the HMA domains of OsHPP09,
405 OsHPP10, OsHPP11 and OsHIPP21, we used isothermal titration calorimetry (ITC).
406 Recombinant AVR-Pia and HMA domains were produced and purified from *E. coli*
407 (**Supplementary Fig. 13**). Titration of AVR-Pia into a solution containing any of the purified
408 HMA domains resulted in negative peaks in the titration curve (**Fig. 5, Supplementary Fig.**
409 **14**), indicative of an exothermic binding interaction. Dissociation constant (K_D) values were

410

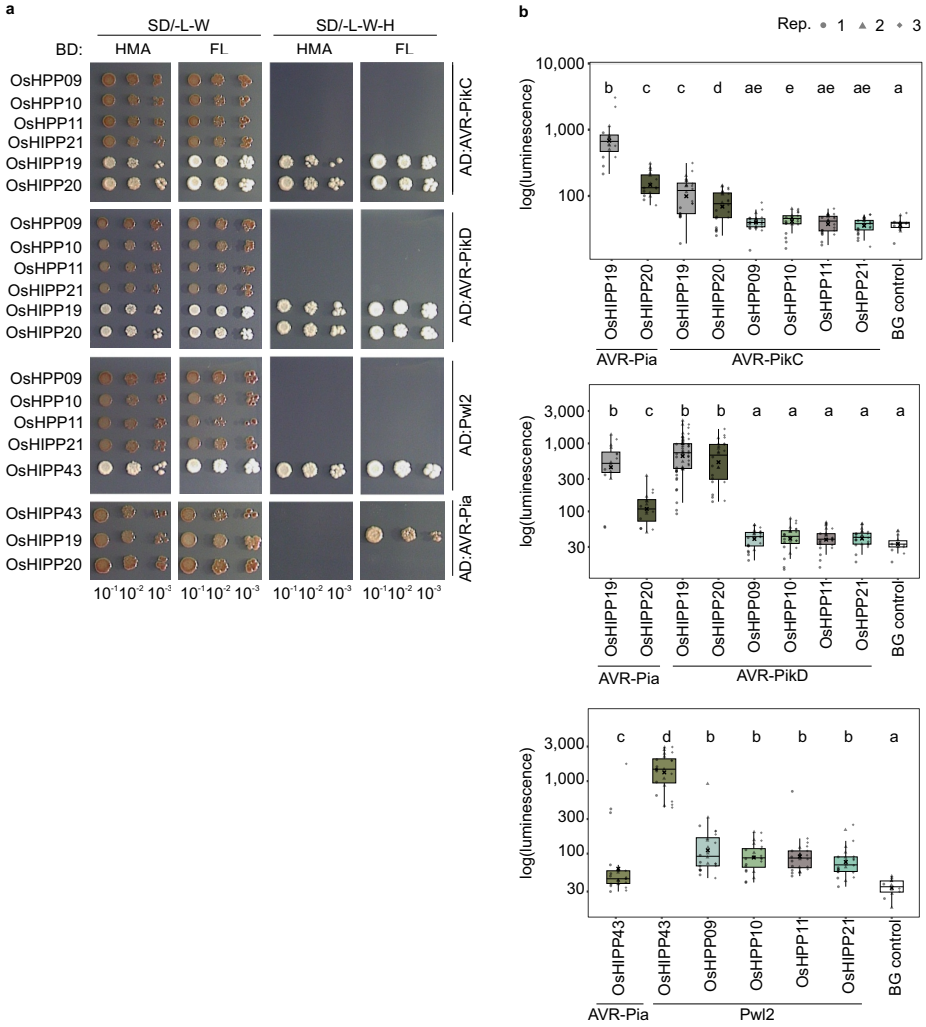

Fig. 4. OsH(I)PPs interacting with AVR-Pia do not interact with AVR-Pik or Pwl2.

a Y2H interaction analysis between AVR-PikC, AVR-PikD, Pwl2 and AVR-Pia and either the heavy metal-associated (HMA) domain or full-length (FL) proteins of OsH(I)PPs. OsHIPP19/AVR-PikC, OsHIPP20/AVR-PikC, OsHIPP19/AVR-PikD, OsHIPP20/AVR-PikD and OsHIPP43/Pwl2 served as positive controls. Serial dilutions of diploid yeast were spotted onto synthetic defined (SD) media to monitor growth (SD/-LW) or to assess protein-protein interactions (SD/-LWH). Photos were taken after 7 days of incubation. AD, activating domain; BD, binding domain. **b** Quantitative measurement of luciferase-derived signals shows that AVR-PikC and AVR-PikD do not interact with OsHPP09, OsHPP10, OsHPP11 and OsHIPP21, while Pwl2 shows weak luminescence signals with these proteins, suggesting weak interactions. AVR-Pia also interacts with OsHIPP19 and OsHIPP20 in planta. MAX effectors were fused to the N-terminal part of luciferase (3xHA:NLuc:MAX) and co-expressed with OsH(I)PP FL proteins fused at their N-termini to the C-terminal part of luciferase (3xFlag:CLuc:OsH(I)PP). Co-expression of AVR-PikC/AVR-PikD with OsHIPP19/20 and Pwl2 with OsHIPP43 served as positive controls, AVR-Pia with OsHIPP43 served as negative control. Leaves infiltrated with P19 alone served as background (BG) control. Leaf discs were collected 2 days post infiltration. Box plots show the median (line), mean (cross) and upper/lower quartiles (box limits), whiskers extend to the most extreme data points within 1.5x the interquartile range. Values outside this range are shown as individual data points. Unless otherwise stated, three independent replicates were performed, with n = 8 per combination per replicate. Due to experimental constraints, the following sample sizes apply to specific conditions: AVR-Pia/OsHIPP19 and AVR-Pia/OsHIPP20 in AVR-PikC and AVR-PikD panels: n = 4 in replicates 1 and 3. BG control in AVR-PikC and AVR-PikD panels: n = 3 in replicates 1 and 3 and BG control

in Pwl2 panel: n = 2 in replicates 1 and 3. AVR-PikD/OsHIPP19 n = 16 in replicates 1 and 3 and n = 24 in replicate 2. Data points are individually plotted and shaped according to the replicate. Different letters indicate statistically significant differences based on a pairwise Wilcoxon test (α = 0.05).

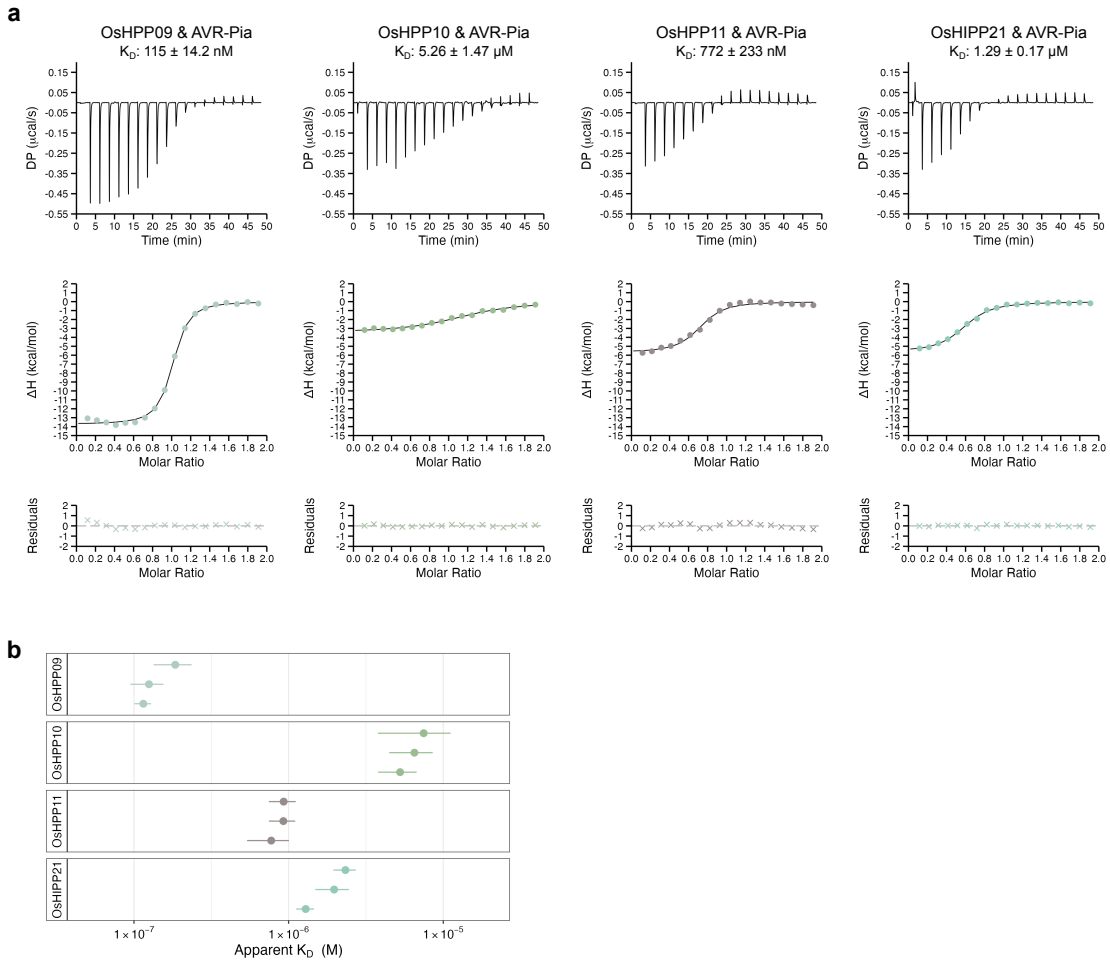

Fig. 5. AVR-Pia binds the HMA domains of OsH(I)PPs with varying affinities.

a Representative ITC experiments for each of the AVR-Pia/HMA interactions tested. Top panel shows the raw thermogram obtained from titration of AVR-Pia into a solution containing the purified HMA domains. Central panel shows the integrated heats (coloured dots) and binding isotherm fitted to a single site model (black line) using the MicroCal PEAQ-ITC analysis software (Malvern Panalytical). Bottom panel shows the differences (coloured crosses) between the modelled and observed values (residuals). **b** Dot plot representation of the apparent KD for each of the AVR-Pia/HMA interactions in three independent experiments. Coloured dots represent the KD vales determined in each replicate with coloured lines representing the error associated with the KD value as determined by the MicroCal PEAQ-ITC analysis software (Malvern Panalytical).

446 determined from binding isotherms (**Fig. 5, Supplementary Fig. 14**) fitted to a single site
447 model.

448 AVR-Pia bound to the HMA domain of OsHPP09 with an apparent K_D of 115 nM (**Fig. 5**).
449 Despite differing in just six amino acids, AVR-Pia bound OsHPP10-HMA with significantly
450 lower affinity, with an apparent K_D of 5.26 µM. The affinities of the interactions of AVR-Pia with
451 OsHPP11-HMA and OsHIPP21-HMA fall between these two extremes, with apparent K_Ds of
452 772 nM and 1.29 µM, respectively. (**Fig. 5, Supplementary Fig. 14, Supplementary Table**
453 **3**). Dissociation constants and thermodynamic parameters and profiles are provided in
454 **Supplementary Table 3 and Supplementary Fig. 15**. The apparent K_Ds, as determined by
455 ITC, for the interactions between OsRGA5-HMA and AVR-Pia or AVR1-CO39 have previously
456 been reported as 7.8 µM [11] and 5.1 µM[10], respectively.

457 **The crystal structure of AVR-Pia in complex with the HMA domain of OsHPP09 reveals**
458 **interface contacts underpinning high affinity binding**

459 To understand the structural basis of the interaction between AVR-Pia and OsHPP09-HMA,
460 we purified and crystallised the effector/HMA complex. Needle-like crystals were obtained in
461 commercial screens and subsequent optimisation of conditions (see Materials and Methods)
462 resulted in crystals suitable for diffractions studies. X-ray diffraction data were collected at the
463 European Synchrotron Radiation Facility (ESRF) to a resolution of 1.65 Å. The structure was
464 solved by molecular replacement and refined and validated as described in the Materials and
465 Methods. Data collection, processing and refinement statistics are presented in
466 **Supplementary Table 4**. The final refined model has been deposited in the Protein Data Bank
467 with accession code 9RSV.

468 As expected, OsHPP09-HMA adopts the well-characterised HMA domain fold, consisting of a
469 four-stranded antiparallel β-sheet and two α-helices arranged with βαββαβ topology (**Fig. 6**).
470 Solution structures of AVR-Pia alone have previously been determined by NMR spectroscopy
471 [4,51] (PDB accession codes 2MYW, 2N37) and the crystal structure of AVR-Pia bound to the
472 integrated HMA domain of the NLR protein OsPikp-1 has also been solved [45] (PDB accession
473 code 6Q76). The structure of AVR-Pia determined here is highly similar (RMSD of 0.357 Å to
474 6Q76, 0.951 Å to 2MYW, and 1.690 Å to 2N37) and adopts the six-stranded β-sandwich
475 structure characteristic of the MAX effector family (**Fig. 6**) [4,5].

476 The global structure of the complex between AVR-Pia and OsHPP09-HMA resembles the
477 previously determined structures of AVR-Pia bound to the HMA ID of OsPikp-1 (PDB 6Q76)
478 and AVR1-CO39 in complex with the HMA ID of OsRGA5 (PDB 5ZNG) (**Supplementary Fig.**
479 **16**). Analysis with qtPISA [52] (**Supplementary Table 5**) determined an interface area of 521.7

480

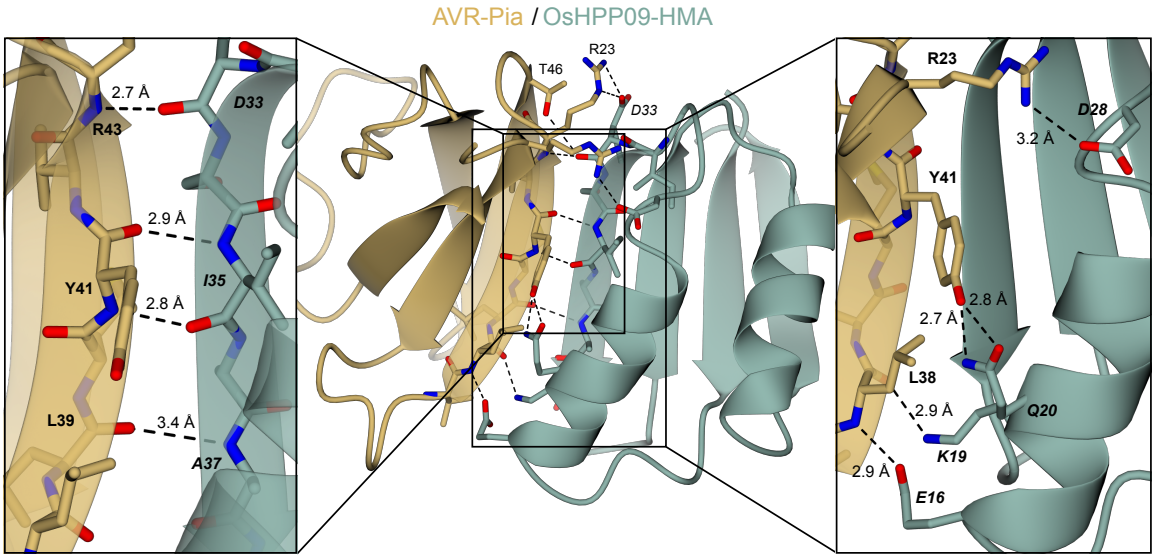

Fig. 6. Crystal structure of the HMA domain of OsHPP09 in complex with AVR-Pia.

The structures of OsHPP09-HMA and AVR-Pia are represented as teal and gold ribbons, respectively. The amino acids comprising β2 of AVR-Pia and β2 of the HMA domain are represented as cylinders. Side chains involved in intermolecular hydrogen bonds/salt bridges are also represented as cylinders. Hydrogen bonds are represented by black dashed lines labelled with the bond length. Left insert shows main chain hydrogen bonds between AVR-Pia-β2 and OsHPP09-β2. Right insert shows intermolecular contacts between side chains of residues in OsHPP09-α1 and AVR-Pia.

489 Å^2, fractionally larger than the 460.7 Å^2 interface between AVR-Pia/OsPikp-HMA and the
490 492.8 Å^2 interface between AVR1-CO39/OsRGA5-HMA. In all three cases, β2 of the MAX
491 effector is aligned in an antiparallel orientation with β2 of the HMA domain, resulting in the
492 formation of an antiparallel β-sheet comprising β6, β1 and β2 of the MAX effector and the four-
493 stranded β-sheet of the HMA domain (**Supplementary Fig. 16a**), with hydrogen bonding
494 between the backbone amine and carbonyl groups of the peptide backbone of the adjacent β-
495 strands (**Supplementary Fig. 16b**).

496 In contrast to the structures of OsPikp-HMA with AVR-Pia and OsRGA5-HMA with AVR1-
497 CO39, where the interface is dominated by main chain hydrogen bonding, in the OsHPP09-
498 HMA/AVR-Pia structure, the side chains of multiple residues in α1 of the HMA domain form
499 intermolecular hydrogen bonds with the effector. The side chains of OsHPP09^{E16} and
500 OsHPP09^{K19} form hydrogen bonds with the peptide backbone of AVR-Pia^{L38} (**Supplementary**
501 **Fig. 16c**). The amino acid in the corresponding position to OsHPP09^{K19} in OsPikp-HMA is
502 OsPikp-1^{R203}, however it is OsPikp-1^{R226}, in the β2-β3 loop, which forms an analogous
503 hydrogen bond with AVR-Pia^{L38} (**Supplementary Fig. 16c**). OsRGA5-HMA has a basic
504 residue (R1012) at the corresponding position to OsHPP09^{K19}, and the side chain of OsRGA5-
505 HMA^{R1012} is orientated towards the side chain of AVR1-CO39^{D35}, however the distance
506 between them (4.1 Å) is greater than the 4 Å cutoff typically used when considering salt bridge
507 interactions (**Supplementary Fig. 16c**). At the start of β2, the side chain of OsHPP09^{D33} forms
508 salt bridge interactions with the side chain of AVR-Pia^{R43} (**Supplementary Fig. 16d**). This
509 aspartate residue is conserved in both OsPikp-HMA (D217), where it similarly forms a salt
510 bridge with AVR-Pia^{R43}, and in OsRGA5-HMA (D1026), where it forms an indirect, water-
511 mediated contact with the backbone of AVR1-CO39^{T41} (**Supplementary Fig. 16d**). The
512 OsHPP09^{Q20} side chain forms hydrogen bonds with the side chain hydroxyl of AVR-Pia^{Y41}
513 (**Supplementary Fig. 16e**). The amino acid in the corresponding position in OsPikp-HMA is
514 serine, and a water-mediated contact is formed between the smaller side chain of OsPikp-
515 HMA^{S204} and the side chain hydroxyl of AVR-Pia^{Y41} (**Supplementary Fig. 16e**). Finally,
516 towards the C-terminal end of OsHPP09-α1, the side chain of OsHPP09^{D28} forms a salt bridge
517 with AVR-Pia^{R23} (**Supplementary Fig. 16f**). By contrast, the corresponding amino acid in
518 OsPikp-1, OsPikp-1^{S212}, forms a hydrogen bond with the side chain hydroxyl of AVR-Pia^{Y85}
519 (**Supplementary Fig. 16f**). Overall, the increased number of intermolecular hydrogen bonds
520 in the AVR-Pia/OsHPP09-HMA structure compared to the structure of AVR1-CO39/OsRGA5-
521 HMA likely explain the reported difference in binding affinities.

522 To validate the interface observed in the crystal structure of OsHPP09-HMA in complex with
523 AVR-Pia, NMR titration with ^{1}H-^{15}N-HSQC NMR spectra of ^{15}N-labelled AVR-Pia alone and in

524 the presence of purified unlabelled OsHPP09-HMA were performed. HSQC spectra for ^{15}N-
525 labelled AVR-Pia had previously been collected and peaks assigned to the protein [4], and these
526 assignments were used in the present study. Binding of AVR-Pia to OsHPP09-HMA alters the
527 chemical environment of the amino acids located at the binding interface, resulting in a change
528 in the chemical shift observed for those amino acids in the HSQC spectra. Depending on the
529 rate of complex formation and dissociation, expressed by the exchange rate constant kex, and
530 the chemical shift difference $\Delta\omega$ between the unbound and bound states ($\Delta\omega$ = difference
531 between the resonance frequencies of the exchanging sites), different exchange regimes
532 occur. NMR titration showed that the AVR-Pia/OsHPP09-HMA complex was in slow exchange
533 with kex << $\Delta\omega$ since separate resonances appeared for individual species. For certain peaks
534 in the spectra of ^{15}N-labelled AVR-Pia with OsHPP09-HMA, it was not possible to confidently
535 identify the corresponding peak in the spectra for ^{15}N-labelled AVR-Pia alone. However,
536 significant changes in chemical shift ($\Delta\delta$ AV > 0.4 ppm) were observed for multiple residues
537 in β2 and β3 of AVR-Pia, consistent with the interface in the crystal structure **(Supplementary**
538 **Fig. 17)**.

539 **Replacement of OsHPP09^{E16} with alanine or arginine disrupts AVR-Pia binding**

540 Next, we aimed to identify point mutations in the HMA domain of OsHPP09 which interfere
541 with AVR-Pia binding. First, using the crystal structure, we selected residues where the side
542 chains contribute intermolecular hydrogen bonds or salt bridges and mutated each residue to
543 alanine (E16A, K19A, Q20A, D28A, D33A) and, for the acidic residues, also to arginine (E16R,
544 D28R, D33R). D33 is conserved in OsHPP09, OsHPP10 and OsHPP11, but also in the HMA
545 IDs of Pikp-1 (D217) and RGA5 (D1026) (**Supplementary Fig. 16C**). By contrast, the residue
546 in the corresponding position in Pikm-HMA, which does not bind AVR-Pia [45], is histidine. We
547 therefore also included the D33H mutation. Second, we used FoldX [53] to predict the effect of
548 mutating each interface residue in OsHPP09-HMA to all other amino acids. Based on the
549 calculated difference of interaction free energy ($\Delta\Delta G$) upon mutation, we selected three further
550 mutations (K19W, I35K, A37W) for experimental characterisation.

551 Mutations were introduced into expression constructs by site-directed mutagenesis. The effect
552 of the mutations on AVR-Pia binding was tested in Y2H experiments. Introduction of the point
553 mutations E16A, E16R, D28A, D28R and I35K in OsHPP09 resulted in a complete loss of
554 interaction with AVR-Pia (**Fig. 7a**). In contrast, the remaining mutations (K19A, K19W, Q20A,
555 D33A, D33H, D33R, A37W) did not completely abolish the interaction (**Fig. 7a**). However,
556 several including K19A, K19W, D33A, D33H, D33R and A37W led to reduced yeast growth
557 on interaction-selective media when co-expressed with AVR-Pia, suggesting a weakening of
558 the interaction compared to the wildtype OsHPP09/AVR-Pia pair. Immunoblot analysis

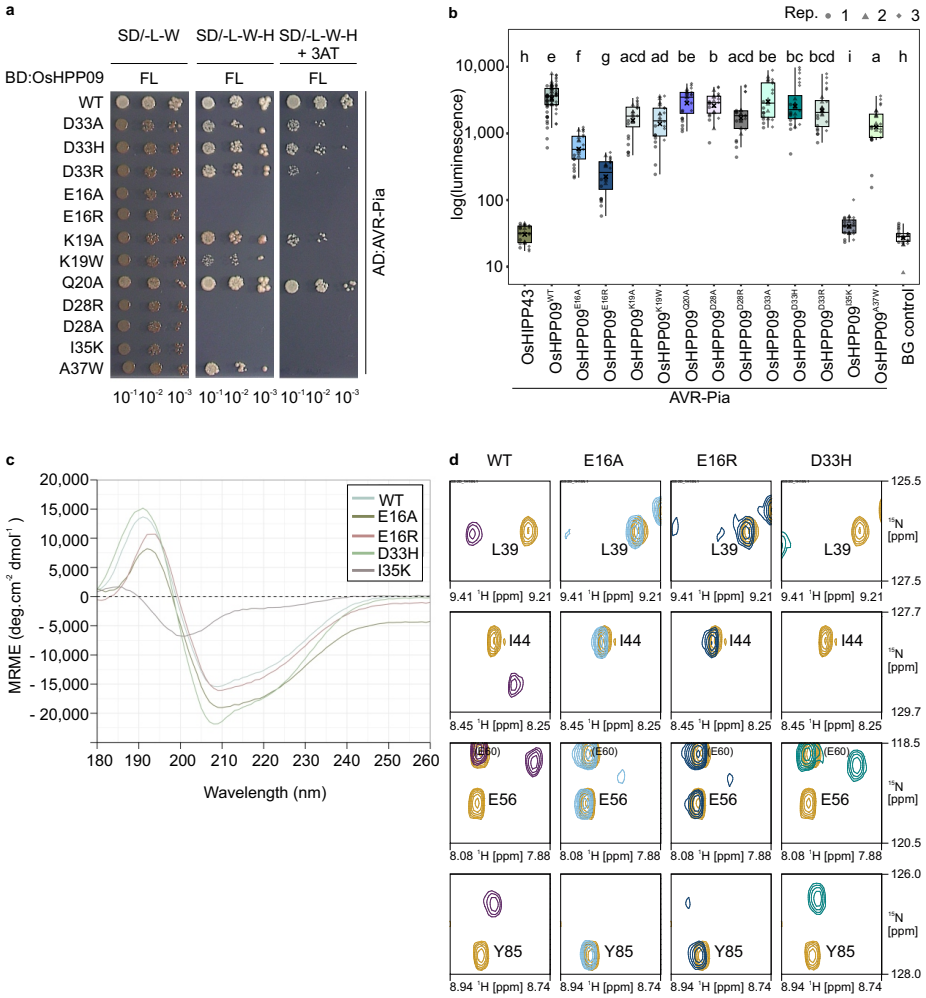

Fig. 7. Mutation of OsHPP09 E16 reduces AVR-Pia binding.

a Y2H interaction analysis between AVR-Pia and full-length (FL) OsHPP09 mutant versions carrying single mutations in the binding interface. OsHPP09^{WT}/AVR-Pia served as positive control. Serial dilutions of diploid yeast were spotted onto synthetic defined (SD) media to monitor growth (SD/-LW) or to assess protein-protein interactions (SD/-LWH and SD/-LWH supplemented with 5 mM 3AT). Photos were taken after 7 days of incubation. AD, activating domain; BD, binding domain. **b** Quantitative measurement of luciferase-derived signals shows that the E16A, E16R and I35K mutations in OsHPP09 significantly reduce its interaction with AVR-Pia in a split-luciferase complementation assay. AVR-Pia was fused to the N-terminal part of luciferase (3xHA:NLuc:AVR-Pia) and co-expressed with OsH(I)PP FL proteins fused at their N-termini to the C-terminal part of luciferase (3xFlag:CLuc:OsH(I)PP). Co-expression of AVR-Pia with OsHPP09 served as positive control, co-expression of OsHIPP43 with AVR-Pia served as negative control. Leaves infiltrated with P19 alone served as background (BG) control. Leaf discs were collected 2 days post infiltration. Box plots show the median (line), mean (cross) and upper/lower quartiles (box limits), whiskers extend to the most extreme data points within 1.5x the interquartile range. Values outside this range are shown as individual data points. Three independent replicates were performed, with n = 8 per combination per replicate. Data points are individually plotted and shaped according to the replicate. Different letters indicate statistically significant differences based on a pairwise Wilcoxon test (α = 0.05). **c** Circular dichroism (CD) spectra obtained for WT OsHPP09-HMA (pale blue) and variants carrying E16A, E16R, I35K or D33H mutations. Negative peaks at 222 nm and 208 nm and a positive peak at 193 nm are indicative of α-helices while a negative peak at 218 nm and positive peak at 195 nm are indicative of β-sheets, consistent

579 with the expected βαββαβ topology of an HMA domain. In the case of the I35K mutant, low ellipticity above 210
580 nm and a negative peak at 200 nm is indicative of disorder. **d** Overlays of cross-peaks from HSQC spectra
581 corresponding to residues L39, I44, E56 and Y85 of ^{15}N-labelled AVR-Pia alone (orange) and in the presence of
582 either WT OsHPP09-HMA or variants carrying E16A, E16R or D33H mutations (blue/green/purple). Overlays of
583 the full spectra are provided in Supp. Figures S19-S21. Chemical shift perturbation of ^{15}N-labelled AVR-Pia is
584 indicative of an interaction with the HMA domain.

585 revealed that the K19A, K19W and I35K mutants exhibited lower protein expression levels,
586 while all other mutant constructs showed similar expression to wildtype OsHPP09
587 (**Supplementary Fig. 3d**).

588 To assess the effect of the mutations in the context of the full-length protein in planta, we
589 performed split-luciferase complementation assays in *N. benthamiana*. The E16A and E16R
590 mutants showed significantly reduced interaction with AVR-Pia, while the I35K mutant
591 completely lost its ability to interact with AVR-Pia, consistent with the Y2H results (**Fig. 7b**). In
592 contrast, the D28A and D28R mutations, which abolished interaction in Y2H assays, had only
593 a minor effect on the interaction with AVR-Pia in planta, similar to the other tested mutants
594 (**Fig. 7b**). Immunoblot analysis demonstrated that all proteins were expressed at comparable
595 levels in planta (**Supplementary Fig. 18**).

596 Next, we aimed to establish whether the E16A, E16R and I35K mutations affect the structure
597 of the HMA domain. OsHPP09^{E16A}-HMA, OsHPP09^{E16R}-HMA and OsHPP09^{I35K}-HMA, as well
598 as OsHPP09^{D33H}-HMA (as a control), were produced in *E. coli* and purified to homogeneity.
599 The molecular weights of the modified HMA domains were confirmed by intact mass
600 spectrometry. To test whether the mutation affects the overall structure of the protein, we first
601 obtained circular dichroism (CD) spectra for the HMA domains. The spectra for native
602 OsHPP09-HMA showed features characteristic of α-helices (negative peaks around 222 nm
603 and 208 nm, positive peak around 193 nm) and β-sheets (negative peak around 218 nm,
604 positive peak around 195 nm) consistent with the HMA domain fold (**Fig. 7c**). While CD
605 spectra obtained for OsHPP09^{E16A}-HMA, OsHPP09^{E16R}-HMA and OsHPP09^{D33H}-HMA were
606 comparable to the spectra obtained for the native protein, OsHPP09^{I35K}-HMA showed features
607 of disorder (low ellipticity above 210 nm and a negative peak around 200 nm) (**Fig. 7c**). These
608 results suggest that the loss of AVR-Pia binding observed for the I35K mutant is likely due to
609 disruption of the HMA domain fold.

610 We obtained ^{1}H-^{15}N-HSQC NMR spectra of ^{15}N-AVR-Pia in the presence of purified unlabelled
611 HMA domains of OsHPP09^{E16A}, OsHPP09^{E16R}, OsHPP09^{D33H} and OsHPP09^{I35K}. The spectra of
612 ^{15}N-AVR-Pia with OsHPP09^{D33H}-HMA was highly similar to the spectra of ^{15}N-labelled AVR-Pia
613 with WT OsHPP09-HMA (**Fig. 7d**, **Supplementary Fig. 19**). By contrast, the spectra of ^{15}N-
614 AVR-Pia with OsHPP09^{E16A} or OsHPP09^{E16R} showed no chemical shift perturbation and
615 superimposed with the spectra of ^{15}N-AVR-Pia alone (**Fig. 7d**, **Supplementary Fig. 20**,
616 **Supplementary Fig. 21**). Taken together, these results demonstrate that E16A and E16R
617 mutations block AVR-Pia binding without disrupting the HMA domain fold.

618

619 ## Discussion

620 The *Magnaporthe oryzae* effector AVR-Pia is a member of the MAX family of sequence-
621 unrelated, structurally conserved effectors. Here, we identified four small HMA domain-
622 containing proteins which are bound by AVR-Pia.

623 **Structural variation between MAX effectors underpins interactions with different host**
624 **targets**

625 AVR-Pia is the third MAX effector which has been shown to interact with H(I)PPs. AVR-Pik
626 was found to interact with the HMA domains of multiple H(I)PPs within a large phylogenetic
627 clade, referred to as "clade A" [17]. By contrast, Pwl2 interacts specifically with OsHIPP43 and
628 its homologs from other grass species [46]. In the present study, we found that AVR-Pia binds
629 to the HMA domains of OsHPP09, OsHPP10, OsHPP11, and OsHIPP21. Neither AVR-Pik
630 nor Pwl2 interacts with these H(I)PPs, demonstrating that AVR-Pia binds a distinct group of
631 H(I)PPs to those previously identified as MAX effector targets.

632 Strikingly, the interactions between each of the three MAX effectors and HMA domains involve
633 distinct interfaces. In the crystal structures of AVR-Pia/OsHPP09-HMA and Pwl2/OsHIPP43-
634 HMA, β2 of the core MAX fold and β2 of the HMA domain are aligned in an antiparallel
635 orientation [46]. Hydrogen bonds between the two β-strands lead to the formation of an
636 antiparallel β-sheet comprising the four β-strands of the HMA domain and β2, β1 and β6 of
637 the MAX fold. When the HMA domains are superposed, the relative positions of β2 of the MAX
638 fold of Pwl2 and AVR-Pia are very similar (**Supplementary Fig. 22**). However, the other β-
639 strands of Pwl2 are shifted compared to AVR-Pia, enabling residues in β3, β4, and the β3- β4
640 loop of the MAX fold to contribute to the HMA-binding interface. By contrast, in the complex of
641 OsHIPP19-HMA/AVR-PikF, an antiparallel β-sheet forms from the four β-strands of the HMA
642 domain and β3, β4 and β5 of the MAX fold, mediated by main chain hydrogen bonding
643 between β3 of the MAX fold of AVR-PikF and β4 of HIPP19-HMA [41]. Furthermore, while AVR-
644 Pia consists solely of the core MAX fold, AVR-Pik has an unstructured extension at the N-
645 terminus, while in Pwl2 the characteristic MAX fold is proceeded by an α-helix and a C-terminal
646 unstructured region. In both cases, these extensions are involved in HMA binding
647 (**Supplementary Fig. 22**). Pwl2^{E89}, in the α-helix, forms a hydrogen bond with OsHIPP43-
648 HMA^{K51}, while the C-terminal unstructured segment of Pwl2 extends across the HMA domain,
649 forming an extensive interface involving both hydrogen bonds and π-stacking interactions.
650 Similarly, the N-terminal extension of AVR-Pik binds OsHIPP19-HMA by forming multiple
651 hydrogen bonds with residues in β3, β2 and the β2- β3 loop of the HMA domain. The interface
652 in the AVR-Pia/OsHPP09-HMA complex is smaller than in AVR-PikF/OsHIPP19-HMA and

653 Pwl2/OsHIPP43-HMA (521.6 Å^2 compared to 1044.3 Å^2 and 1965.2 Å^2, respectively) and
654 formed almost exclusively by residues in β2 of the core MAX fold.

655 It is interesting that at least three MAX effectors have evolved to bind HMA domains in different
656 ways. This highlights how structural variation within this effector family can underpin different
657 interactions with host targets. At present, the impacts of effector binding to H(I)PPs are
658 unclear, and it remains to be seen whether binding to different interfaces leads to different
659 outcomes.

660 While AVR-Pia, AVR-Pik and Pwl2 all target OsH(I)PPs, AvrPiz-t is reported to interact with
661 diverse host proteins, including rice E3 ubiquitin ligases [54,55], a potassium channel [56], a bZIP-
662 type transcription factor [57] and a nucleoporin [58]. This suggests that MAX effectors may target
663 many different host proteins and processes during infection.

664 **The HMA domains of the OsH(I)PPs bound by AVR-Pia share limited sequence**
665 **similarity with the HMA-ID of OsRGA5**

666 AVR-Pia is recognised by the paired rice NLR immune receptors OsRGA5 and OsRGA4
667 through direct binding of the effector to a non-canonical HMA domain integrated into OsRGA5
668 [9]. The integrated domain model [13] posits that such non-canonical domains originated in the
669 host targets of effectors, and were incorporated into NLR proteins to function as effector
670 "sensors". Consistent with this, the crystal structure of AVR-Pia/OsHPP09 revealed that AVR-
671 Pia binds OsHPP09-HMA and OsRGA5-HMA through similar interfaces [11].

672 AVR1-CO39 is also recognised by direct binding to the HMA ID of OsRGA5. However, AVR1-
673 CO39 did not interact with the same OsH(I)PPs as AVR-Pia. AVR1-CO39 also did not interact
674 with the "clade A" OsH(I)PPs bound by AVR-PikD [17]. AVR1-CO39 is broadly absent from rice-
675 infecting isolates of *M. oryzae* [6,59,60]and loss of this effector has potentially contributed to a
676 host shift from foxtail millet (*Setaria* sp.) to rice. It is therefore possible that AVR1-CO39 has
677 evolved to target H(I)PPs from other grass species, and does not interact with those present
678 in rice.

679 Interestingly, phylogenetic analysis based on HMA domains clusters OsRGA5-HMA with the
680 H(I)PPs targeted by AVR-Pik and the HMA ID of OsPik-1, and not with OsHPP09, OsHPP10,
681 OsHPP11, and OsHIPP21 [17]. We observed interaction between AVR-Pia and FL OsHIPP19,
682 but not with the HMA domain alone, in low stringency Y2H experiments and split-luciferase
683 assays. This suggests that the C-terminal part of OsHIPP19 contributes to AVR-Pia binding
684 and merits further study.

685 Previously published ITC experiments showed that AVR-Pia binds OsRGA5-HMA with a K_D
686 of 7.8 μM [11]. This is comparable to the binding affinity of AVR-Pia to OsHPP10-HMA
687 determined in the present study, but at least one order of magnitude weaker than the
688 interaction between AVR-Pia and OsHPP09-HMA. This higher affinity binding can be
689 explained by the number of intermolecular hydrogen bonds and salt bridges at the interface
690 between AVR-Pia and OsHPP09; while no experimental structure is available for AVR-Pia
691 bound to OsRGA5-HMA, available structures of AVR1-CO39/OsRGA5-HMA and AVR-
692 Pia/OsPikp-HMA, combined with modelling approaches, suggest that the AVR-Pia/OsRGA5-
693 HMA interface likely involves fewer intermolecular contacts. A similar pattern was previously
694 reported for AVR-Pik/HMA interactions; surface plasmon resonance experiments showed that
695 AVR-PikD interacts with the HMA domain of OsHIPP19 with higher affinity than the HMA ID
696 of OsPik-1 [41].

697 It is important to note that these binding affinities are determined in vitro using the purified
698 HMA domain. These experiments therefore lack the biological context of the FL protein or the
699 plant cell environment. In the case of the AVR-Pia/OsRGA5 interaction, regions outside of the
700 OsRGA5 HMA domain contribute to AVR-Pia binding, and it is possible that AVR-Pia also
701 interacts with the C-terminal regions of the OsH(I)PPs. While the AVR-Pia/OsRGA5-HMA
702 interaction may be of lower affinity than the AVR-Pia/OsHPP09-HMA interaction, it is sufficient
703 for OsRGA5/OsRGA4 to activate immune signalling. A higher affinity interaction is unlikely to
704 confer any additional evolutionary benefit to the plant. If OsRGA5 recognises other pathogen
705 effectors, mutations which increase affinity for AVR-Pia may come at the cost of reducing
706 affinity/binding to other effectors.

707 **H(I)PPs are targeted by diverse pests and pathogens, though their precise function in**
708 **plant susceptibility/resistance remains unclear**

709 H(I)PPs, which form extensive families in plants [20,24,25], have been reported to be involved in
710 intracellular metal transport and homeostasis, responses to cold and drought stress and
711 tolerance to heavy metals. In addition to the interactions between *M. oryzae* MAX effectors
712 and OsH(I)PPs, there are a growing number of reports of plant H(I)PPs targeted by proteins
713 from other pests and pathogens. For example, the putative effector RsMf8HN from the
714 necrotrophic fungus *Rhizoctonia solani* interacts with OsHIPP28 [36], while a HIPP from
715 sugarcane (ScPi21) is a target for the *Fusarium sacchari* effector Fs00367 [33]. CsHIPP03 was
716 identified in a Y2H screen as a putative target of the core effector SDE34 secreted by
717 *Candidatus* Liberibacter asiaticus (CLas), a phloem-colonising bacteria which causes citrus
718 huanglongbing disease [38]. An effector secreted by the root-knot nematode *Meloidogyne*
719 *graminicola* binds rice OsHPP04 and suppresses a flg22-induced ROS burst [34]. Finally, the

720 potato mop-top virus (PMTV) movement protein TGB1 interacts with NbHIPP26 to promote
721 the spread of the virus through the plant [29]. Together, these results suggest that the
722 manipulation of H(I)PPs is required for successful infection by diverse pests and pathogens.
723 In spite of this, little is known about the molecular mechanisms through which H(I)PPs affect
724 plant resistance/susceptibility.

725 HMA domains typically coordinate metal ions via two cysteine residues in a MxCxxC motif
726 positioned between α1 and β2. Intriguingly, the metal-binding motif is degenerate in all four
727 HMA domains bound by AVR-Pia, with both cysteines replaced by other amino acids
728 (MTDEKT in OsHPP09, MTDDKI in OsHPP10, MSDTKM in OsHPP11 and MTDERK in
729 OsHIPP21), presumably indicating a lack of metal-binding activity by these proteins.
730 Consistent with this, no electron density suggestive of bound metal ions were observed in the
731 crystal structure of OsHPP09-HMA in complex with AVR-Pia. Interestingly, OsHPP09^{E16},
732 which is important for AVR-Pia binding, is located in the degenerate metal binding motif. Of
733 the clade A H(I)PPs bound by AVR-Pik, some contain an intact MxCxxC motif, while others
734 (such as OsHIPP19 and OsHIPP20) lack one or both cysteine residues. OsHIPP43 has an
735 intact MxCxxC motif, though it has not been established whether it binds metal ions in planta.
736 In cases where HMA domains lack a complete MxCxxC motif, and presumably also lack the
737 capacity to bind metals, the functions of the H(I)PPs are particularly intriguing. They may have
738 acquired entirely new functions outside metal transport and homeostasis, with the stable core
739 fold of the HMA domain supporting diversification of surface properties for new functions.

740 HIPPs and HPPs differ in the presence or absence of a CaaX isoprenylation motif at the C-
741 terminus. Correspondingly, OsHIPP21 has a CaaX motif (CCQM) while no such motif is
742 present in OsHPP09, OsHPP10 or OsHPP11. Protein prenylation can affect subcellular
743 localisation, protein stability, and protein-protein interactions [61]. Several HIPPs have been
744 found to localise to plasmodesmata, with the localisation being dependent on an intact CααX
745 motif [29,32,62]. It is therefore plausible that OsHIPP21 differs in localisation and/or function from
746 the three HPPs, and AVR-Pia interaction may also have different consequences. Further
747 investigation is required to establish both the function of these proteins in planta, and the effect
748 of AVR-Pia binding.

749 **A foundation for precision engineering of effector targets for disease resistance**

750 Pathogens require certain host factors to establish a successful infection, with the underlying
751 genes typically referred to as S genes. Previous studies have shown that *OsHIPP05* (*Pi21*)
752 and *OsHIPP20* are S genes for blast infection; *oshipp05* and *oshipp20* CRISPR-Cas9
753 knockout plants exhibited increased resistance. Further, a recent study reported that

754 overexpression of *HvHIPP43* increased susceptibility to *M. oryzae,* which suggests that
755 *HvHIPP43* may also be a S gene [17,31,32,63–65]. In addition, other H(I)PPs have been reported to
756 be S genes for diverse pests and pathogens. *Arabidopsis thaliana* plants carrying loss-of-
757 function mutations in *AtHIPP27* or *AtHMAD* (also known as *AtHIPP40* [27]) exhibited reduced
758 susceptibility to the beet cyst nematode *Heterodera schachtii* [30] and the bacterial pathogen
759 *Pseudomonas syringae* [39], respectively. Silencing of *TaHIPP1* in wheat reduced sporulation
760 of the wheat stripe rust fungus *Puccinia striiformis f. sp. tritici* [37]. It is possible that *OsHPP09*,
761 *OsHPP10*, *OsHPP11* and/or *OsHIPP21* may also be S genes for rice blast disease, and
762 deletion of these genes may increase blast resistance.

763 While knocking out S genes has the potential to confer durable resistance, it can cause
764 undesirable pleiotropic effects on plant growth and development [66–69]. Advances in genome
765 editing technologies enable specific mutation of genes to alter amino acids in a target protein.
766 This precise approach reduces the likelihood of compromising the endogenous function of the
767 protein [70]. Furthermore, it was recently demonstrated that the virulence function of the MAX
768 effector Pwl2 depends on interaction with OsHIPP43 [32].The function of OsHPP09, and the
769 consequences of AVR-Pia binding, are unknown. However, preventing AVR-Pia binding to
770 OsHPP09 could compromise the function of the effector in promoting disease. In this study,
771 we have demonstrated that a single point mutation in OsHPP09, converting the glutamate in
772 position 16 to either alanine or arginine, is sufficient to prevent AVR-Pia binding. We also
773 found that OsHPP09 carrying an I35K mutation also lost interaction with AVR-Pia. However,
774 while we could produce and purify the recombinant HMA domain from *E. coli*, circular
775 dichroism experiments revealed that this mutation interfered with the correct folding of the
776 HMA domain, indicating that protein misfolding causes the observed loss of AVR-Pia binding.
777 This illustrates the importance of characterising the effects of mutations on protein structure
778 before commencing time-consuming and costly base editing experiments in plants.

779 In summary, we have characterised the interactions between AVR-Pia and a novel subset of
780 HMA domain-containing rice proteins. Biophysical and structural analyses guided
781 mutagenesis of these effector targets, and identified a mutation which blocks effector binding
782 without compromising structural integrity of the HMA domain. This provides a foundation for
783 targeted modification of these proteins for enhanced disease resistance.

784 # Methods

785 ## Cloning

786 The coding sequences (CDS) of *OsH(I)PPs*, including the stop codon, were synthesised by
787 Twist Bioscience. The CDS of *OsHIPP14*, *OsPi21*, *OsHIPP19*, *OsHIPP21* and *OsHPP09* were
788 codon-optimized to enable synthesis.

789 For Y2H and split luciferase experiments, synthesised *OsH(I)PP* genes were used as template
790 for amplification with primers containing *attB1* and *attB2* recombination sites (**Supplementary**
791 **Table S6**) and Phusion High-Fidelity DNA Polymerase (Thermo Fisher Scientific). The
792 resulting PCR products were subsequently introduced into the pDONR207 vector (Invitrogen)
793 via Gateway® BP recombination (Thermo Fisher Scientific). Entry constructs for the MAX
794 effectors dSP-AVR-Pia [13], dSP-AVR1-CO39 [10], dSP-AVR-PikD [44] and dSP-Pwl2 [11] were
795 previously published. The dSP-AVR-PikC fragment was amplified from pCambia1300_dSP-
796 AVR-PikC [50] and dSP-MAX58 from a synthesised gene, both using primers containing *attB1*
797 and *attB2* recombination sites (Supplementary Table S6) and Phusion High-Fidelity DNA
798 Polymerase (Thermo Fisher Scientific). The resulting PCR products were also cloned into the
799 pDONR207 vector (Invitrogen) via Gateway® BP recombination (Thermo Fisher Scientific).

800 For recombinant protein production in *E. coli,* synthesised genes were used as templates for
801 PCR amplification of the HMA domains (**Supplementary Table S1**) with primers containing
802 *Bpi*I restriction sites (**Supplementary Table S6**) using CloneAmp™ HiFi PCR Premix
803 (Clontech Laboratories). The resulting PCR products were introduced into the vector
804 pICH41308 (Addgene #47998; [71]) by Golden Gate assembly [72] to generate level 0 CDS
805 modules. The CDS of OsHIPP21-HMA was codon-optimised for expression in *E. coli* and
806 supplied with the appropriate overhangs and restriction sites for direct assembly into the vector
807 pICH41308 without PCR amplification. The level 0 CDS modules were used in Golden Gate
808 reactions with the pOPIN-GG vector pPGN-C (Addgene #174578, [73]) and the level 0 module
809 pICSL30015 (Addgene #174582, [73]) to generate *E. coli* expression constructs with a cleavable
810 N-terminal 6xHis-MBP tag.

811 Site-directed mutagenesis of OsHPP09-HMA for Y2H, split luciferase, and recombinant
812 protein production was carried out using a QuikChange Site-Directed Mutagenesis Kit
813 (Agilent). To introduce mutations in the prenylation motif of OsHIPPs in the pDONR constructs
814 to generate *OsHIPP14*^{C187S}, *OsHIPP21*^{C133S}, *OsHIPP39*^{C190S}, *OsHIPP41*^{C152S}, and *AVR-Pia-*
815 *H3*, site-directed mutagenesis PCR was carried out using Phusion High-Fidelity DNA
816 Polymerase (Thermo Fisher Scientific) and mutation-specific primers listed in **Supplementary**
817 **Table S6**.

818 Gateway® LR recombination using LR Clonase® II mix (Thermo Fisher Scientific) was used
819 to transfer *OsH(I)PPs* and *RGA5$_{Cter}$* [9] (883-1116 aa) into Gateway®-compatible destination
820 vectors, including a modified Y2H vector pGBKT7-GW [74] and the plant expression vector
821 pBIN-35S-3Flag-Cluc-GWY (Deslandes et al., unpublished). Similarly, MAX effector
822 pDONR constructs were recombined into a modified pGADT7-GW [74] and pBIN-35S-3HA-
823 Nluc-GWY (Deslandes et al., unpublished) destination vectors. The pBIN-35S-3HA-Nluc-
824 GWY and pBIN-35S-3Flag-Cluc-GWY vectors were generated by the ligation of a 3HA-Nluc-
825 FrameB or 3Flag-Cluc-FrameB fragment, respectively, into a XhoI/XbaI digested pBIN-35S
826 vector.

827 Previously published expression constructs for AVR1-CO39, AVR-Pia and AVR-Pia-H3 [4,10,11]
828 were used for protein production in the present study.

829 A complete list of plasmids used in this study is provided in **Supplementary Table S7.**

830 **Yeast two-hybrid**

831 The yeast strain Y2HGold (mating type a; Takara Bio) was transformed with the bait construct
832 expressed from the pGBKT7 vector, which contains the GAL4-BD and the *TRP1* marker gene.
833 These constructs included previously described HMA domains [47], as well as newly generated
834 constructs: OsHIPP21-HMA, OsH(I)PP^{WT} FL and OsH(I)PP$^{C/S}$ FL. The yeast strain Y187
835 (mating type α; Takara Bio) was transformed with the prey construct (MAX effectors)
836 expressed from the pGADT7 vector, which carries the GAL4-AD and the *LEU2* marker
837 gene. Yeast transformation was performed using a lithium acetate (LiAc)-based protocol
838 according to the Yeastmaker Yeast Transformation System (Takara Bio). Transformed yeast
839 cells were plated on synthetic defined (SD) media lacking either tryptophan (-W) or leucine (-
840 L) and incubated at 30 °C for 3 days.

841 Mating of the transformed yeast strains was carried out following the Matchmaker Gold Yeast
842 Two-Hybrid System User Manual (Takara Bio). Diploid yeast cells were selected on SD/-L-W
843 plates (SD medium lacking leucine and tryptophan) after incubation at 30 °C for 2 days. For
844 the Y2H assay, diploid yeast cells were inoculated in SD/-L-W medium, grown for 24 hours at
845 28°C with shaking at 100 rpm, then pelleted and washed twice with sterile water. Serial 10-
846 fold dilutions (10^{-1}, 10^{-2}, and 10^{-3}) were prepared and spotted onto SD selection plates: SD/-
847 L-W (growth control), SD/-L-W-H (lacking leucine, tryptophan, and histidine), SD/-L-W-H
848 supplemented with varying concentrations of 3-amino-1,2,4-triazole (3AT). Plates were
849 incubated at 30 °C for 7 days and subsequently photographed using the presentation station
850 UF-130DX (Samsung).

851 **Yeast two-hybrid cDNA library screening**

852 The Y2H cDNA library derived from the rice cultivar CO39, as well as the BD:dSP-AVR-Pia
853 construct, have been previously described [9,44]. Library screening was conducted following the
854 Matchmaker Gold Y2H system protocol (Takara Bio). Mating was performed between the Y2H
855 Gold strain harbouring GAL4-BD:AVR-Pia and the Y187 strain carrying the CO39 cDNA
856 library. Diploid yeasts were plated on SD/-L-W-H medium and supplemented with 20 mM 3AT.
857 Colonies that grew were re-streaked onto fresh SD/-L-W-H medium containing 20 mM 3AT to
858 confirm interaction-dependent growth. Yeast colony PCR was used to amplify the cDNA
859 inserts from positive clones, and PCR products were sequenced. The resulting sequences
860 were aligned to the Nipponbare rice genome using BLAST to identify the corresponding genes.
861 Only genes for which the cDNA inserts (or fragments of cDNAs) were cloned in-frame with the
862 GAL4-AD were retained as candidate AVR-Pia targets.

863 **Agrobacterium-mediated transient expression in *N. benthamiana***

864 *Agrobacterium tumefaciens* strains AGL1 (carrying split-luciferase constructs) and GV3101-
865 pMP90 (carrying 35S::P19) were grown overnight at 28°C in 5 mL LB medium supplemented
866 with the appropriate antibiotics. Overnight cultures were pelleted at 4,000 x *g* for 10 minutes,
867 and the pellets were resuspended in 2 mL infiltration buffer (10 mM $MgCl_2$, 10 mM MES pH
868 5.6, 150 µM acetosyringone). The bacterial suspensions were incubated in the dark for 2
869 hours. The optical density at 600 nm (OD_{600}) was adjusted to 0.05 for 35S::P19 and 0.1 for
870 OsH(I)PPs and MAX effectors, respectively. In all infiltration mixes, 35S::P19 was co-infiltrated
871 to suppress gene silencing. Agrobacterial suspensions were mixed accordingly and infiltrated
872 into the leaves of 5–6-week-old *N. benthamiana* plants using a needleless syringe. Leaf discs
873 were harvested 2 days post-infiltration for luminescence measurements or protein extraction.
874 *N. benthamiana* plants were grown in a growth chamber on soil under a 16-hour light / 8-hour
875 dark cycle, at 20 °C and 65 - 75% relative humidity.

876 **Split luciferase assay**

877 For luminescence measurements, 4-mm leaf discs were collected using a Miltex Biopsy Punch
878 (Delta Microscopie) and individually placed into wells of a white 96-well plate containing water.
879 The water was removed and replaced with a 1 mM Xenolight D-luciferin-K^+ salt bioluminescent
880 substrate solution (Perkin Elmer). Luminescence was quantified using a Spark® microplate
881 reader (Tecan) over three cycles of 10 minutes each. For all experiments, data from the third
882 cycle were used for analysis. Each interaction was tested with eight technical replicates (eight
883 leaf discs per plate from four individual plants per biological replicate, unless otherwise
884 indicated in the figure legend). The luminescence assay was performed in three independent
885 experiments. Statistical analyses from three independent replicates (typically involving 24 leaf

886 discs in total, unless otherwise indicated in the figure legend) and data visualization were done
887 using R (version 4.4.1). Multiple comparisons were performed using pairwise Wilcoxon tests
888 followed by a Benjamini-Hochberg p-value adjustment with the stats package. Boxplots were
889 generated using the ggplot2 package.

890 **Protein extraction and Western blotting**

891 Protein extraction from yeast was performed using a post-alkaline extraction protocol, as
892 described by Kushnirov [75]. For BD-OsHIPP14/19/20/39/41 and AD-MAX, yeast crude extracts
893 were resuspended in 50 µL of 1x LDS loading buffer (1x Bolt™ LDS sample buffer (Thermo
894 Fisher Scientific), 1x NuPAGE™ sample reducing agent (Thermo Fisher Scientific)), boiled at
895 95°C for 10 minutes, and loaded onto a 10% NuPAGE™ Bis-Tris gels (Invitrogen). For BD-
896 OsHPP09/10/11 and OsHIPP21, yeast crude extracts were resuspended in 50 µL of 1x SDS-
897 Tricine buffer (1x SDS-Tricine buffer (Thermo Fisher Scientific), 1x NuPAGE™ sample
898 reducing agent (Thermo Fisher Scientific)) and boiled at 85 °C for 2 minutes before loading
899 onto a 10-20% Tricine gel (Novax). Proteins were transferred to iBlot® nitrocellulose
900 membrane (Invitrogen) using the iBlot 2 Gel Transfer Device (program: 20 V 1 min, 23 V 4
901 min, 25 V, 2 min, Thermo Fisher Scientific), and analysed by immunoblotting.

902 For protein extraction from *N. benthamiana*, four leaf discs (0.8 mm diameter) were collected,
903 immediately frozen in liquid nitrogen and ground using a tissue homogenizer (Retsch GmbH).
904 The ground plant material was solubilized in 200 µL extraction buffer (20 mM Tris-Hcl pH 7.5,
905 150 mM NaCl, 1 mM EDTA pH 8.0, 1% Triton X-100, 0.1% SDS, 5 mM DTT, 1x Protease
906 inhibitor cocktail (Sigma-Aldrich), 1x EDTA-free cOmplete protease inhibitor (Roche)). Protein
907 extracts were centrifuged at 18,000 x *g* for 15 minutes at 4 °C, and the resulting supernatants
908 were collected. 2x LDS buffer (Bolt™ LDS sample buffer (Thermo Fisher Scientific) and
909 NuPAGE™ sample reducing agent (Thermo Fisher Scientific)) was added and samples were
910 denatured at 70 °C for 10 minutes. Proteins were then resolved by electrophoresis on
911 NuPAGE™ 4-12% Bis-Tris gels (Invitrogen). Proteins were transferred to iBlot® nitrocellulose
912 membrane (Invitrogen) using the iBlot 2 Gel Transfer Device (program: 20 V 1 min, 23 V 4
913 min, 25 V, 2 min, Thermo Fisher Scientific), and analysed by immunoblotting.

914 For immunodetection of proteins, rabbit anti-GAL4-BD (sc-577, Santa Cruz Biotechnology,
915 1:2,000), goat anti-rabbit IgG-HRP (1:20,000, Sigma-Aldrich, A0545), mouse anti-Flag M2-
916 HRP (1:60,000, Sigma-Aldrich) and rat anti-HA-HRP (clone 3F10, 1:1,1000, Roche) were
917 used. Chemiluminescence was detected using the Immobilon western kit (Millipore) or the
918 SuperSignal™ West Femto Maximum Sensitivity substrate (Thermo Fisher Scientific) and the
919 Syngene 680X EF GBOX imaging system (Syngene).

920 **Protein production and purification**

921 ***HMA domains***

922 HMA domains were produced with a cleavable N-terminal 6xHis-MBP tag from *E. coli* BL21
923 (DE3) or BL21 (DE3) pLysS. 700 mL cell cultures were grown in LB media at 37 °C from a
924 starting OD_{600} of 0.05-0.07 to an OD_{600} of 0.5-0.8. Protein production was induced by addition
925 of IPTG (final concentration 1 mM) and cell cultures were grown for a further 14-16 hours at
926 20 °C. Cells were harvested by centrifugation and the pellets stored at -70 °C prior to
927 purification. The pellets were then thawed and resuspended in 50 mM Tris-HCl pH 7, 300 mM
928 NaCl, 30 mM imidazole supplemented with cOmplete EDTA-free protease inhibitor cocktail
929 (Roche). Cells were lysed by sonication and the lysate clarified by centrifugation at 40,000 x
930 *g* at 6 °C for 30 minutes to pellet insoluble material, then the supernatant was filtered (0.45
931 µm). All subsequent affinity chromatography and size exclusion chromatography steps were
932 carried out with an ÄKTA Pure system (Cytiva) at 4 °C. The filtered supernatant was applied
933 to a 5 ml HisTrap™ FF column (Cytiva) and, following washing with 50 mM Tris-HCl pH 7, 300
934 mM NaCl, 30 mM imidazole, bound protein was step-eluted with 50 mM Tris-HCl pH 7, 300
935 mM NaCl, 500 mM imidazole. The eluate was injected onto a Superdex 75 26/60 size
936 exclusion chromatography column (Cytiva) pre-equilibrated in 50 mM Tris-HCl pH 7, 150 mM
937 NaCl. Fractions containing the fusion protein were combined and incubated with 3C protease
938 overnight at 4 °C. The HMA domains were separated from the 6xHis-MBP fusion tag and GST-
939 tagged 3C protease by injecting the protease-treated sample onto a 5 ml HisTrap™ FF column
940 (Cytiva), 5 ml MBPTrap™ HP column (Cytiva), and 5 ml GSTrap™ HP column (Cytiva)
941 connected in tandem and equilibrated in 50 mM Tris-HCl pH 7, 300 mM NaCl, 30 mM
942 imidazole. Fractions containing the HMA domains were pooled and concentrated to < 8 ml
943 then injected onto a Superdex 75 26/60 size exclusion chromatography column (Cytiva) pre-
944 equilibrated in 50 mM Tris-HCl pH 7, 150 mM NaCl. Fractions containing the purified HMA
945 domains were combined and concentrated. At each stage, fractions containing the HMA
946 domain were determined by SDS-PAGE. Samples were combined with 5X SDS loading buffer
947 (60 mM Tris-HCl pH 6.8, 25% glycerol, 4% SDS, 0.1% bromophenol blue, 10 mM DTT) and
948 heated at 95 °C for 5 minutes, then loaded onto a Bolt™ 10 %, Bis-Tris gel (Invitrogen). After
949 migration, gels were stained in InstantBlue® Coomassie protein stain (Abcam). Final protein
950 concentration was determined using a Pierce™ BCA Protein Assay Kit (ThermoFisher
951 Scientific), due to the extreme molar extinction coefficients of the proteins (0 $M^{-1}cm^{-1}$ for
952 OsHIPP21-HMA, 1490 $M^{-1}cm^{-1}$ for OsHPP-HMA domains) at 280 nm. Proteins were stored at
953 -80 °C.

954 ***MAX effectors***

955 AVR-Pia, AVR-Pia-H3 and AVR1-CO39 were produced and purified as previously described
956 [4,10,11]. Concentrations of the MAX effectors were determined from their molar extinction
957 coefficients and their absorbance at 280 nm.

958 **Analytical size exclusion chromatography**

959 Analytical size exclusion chromatography experiments were conducted using a Superdex 75
960 10/300 GL column (Cytiva) connected to an ÄKTA Pure system (Cytiva) at 4 °C. The running
961 buffer was 50 mM Tris pH 7, 150 mM NaCl, 1 mM DTT for experiments with AVR1-CO39 and
962 20 mM sodium citrate pH 5.6, 150 mM NaCl, 1 mM DTT for experiments with AVR-Pia and
963 AVR-Pia-H3. To investigate whether OsHPP09-HMA forms a complex with the effectors, the
964 two proteins were combined in a 1:1 molar ratio and incubated on ice for 1 h prior to analysis.
965 Each protein was also analysed alone, at a concentration equivalent to that present in the
966 mixture. For each experiment, 100 µl protein was injected onto the column. Elution was carried
967 out at a flow rate of 0.5 ml/min, and 500 µl fractions were collected for analysis by SDS-PAGE.
968 Samples were combined with 5X SDS loading buffer (60 mM Tris-HCl pH 6.8, 25% glycerol,
969 4% SDS, 0.1% bromophenol blue, 10 mM DTT) and heated at 95 °C for 5 minutes, then loaded
970 onto a Bolt™ 10 %, Bis-Tris gel (Invitrogen). After migration, gels were stained in InstantBlue®
971 Coomassie protein stain (Abcam).

972 **Circular dichroism spectroscopy**

973 Circular dichroism (CD) spectra were obtained using a Chirascan™ CD Spectrometer (Applied
974 Photophysics). The temperature of the sample compartment was set to 20 °C. Proteins were
975 dialysed into 10 mM sodium phosphate, pH 7.2 using Slide-A-Lyzer™ MINI dialysis devices
976 (Thermo Fisher Scientific). 40 µl protein was used to fill a 0.1 mm cuvette. Spectra were
977 obtained for wavelengths from 180 nm to 260 nm with a step size of 1 nm, bandwidth of 2 nm
978 and time-per-point of 2 s. Ten spectra were acquired for buffer and for each sample. The
979 average trace for the buffer was subtracted from the average trace for each protein. Units
980 were converted from millidegrees to mean residue molar ellipticity (MRME) using the equation:

981 $$MRME = \frac{millidegrees \times MRW}{10 \times L \times C}$$

982 where L = path length (cm), C = protein concentration (mg/ml), and MRW = mean residue
983 weight, determined as:

984 $$MRW = \frac{molar\ mass}{(number\ of\ amino\ acids - 1)}$$

985

986 **Nuclear magnetic resonance titration**

987 Samples of ^{15}N-labelled AVR-Pia (40 μM) alone and in a 1:1 molar ratio with unlabelled
988 OsHPP09-HMA, or OsHPP09-HMA mutants, were prepared in 20 mM sodium citrate, pH 5.6,
989 150 mM NaCl and 1mM DTT. HSQC spectra were recorded at 305K on a Bruker Avance 800
990 MHz spectrometer equipped with a triple resonance (^{1}H, ^{15}N, ^{13}C) z-gradient cryo-probe.
991 Chemical shift differences were measured from the HSQC spectra of AVR-Pia alone and the
992 AVR-Pia/OsHPP09-HMA complex. All spectra are referenced to the internal reference DSS
993 for the ^{1}H dimension and indirectly referenced for the ^{15}N dimension [76]. Spectra were
994 processed using Topspin (v. 3.2) and analyzed using strip-plots with Cindy in house software
995 and CCPN [77] [analysis v 2.3]. The ^{1}H, ^{15}N assignments were derived by analogy from the
996 assignments of AVR-Pia wildtype. All the NMR samples were prepared with addition of 10%
997 D_2O and 1 μM DSS as a reference.

998 **Isothermal titration calorimetry**

999 ITC experiments were performed using a MicroCal PEAQ-ITC (Malvern Panalytical). Proteins
1000 were dialysed overnight into the experiment buffer (20 mM sodium citrate pH 6.0, 150 mM
1001 NaCl, 1 mM TCEP). Experiments were carried out 25 °C with a reference power of 5 μcal/s.
1002 The calorimetric cell was filled with the purified HMA domain at 18 μM (OsHPP09-HMA), 35
1003 μM (OsHIPP21-HMA and OsHPP11-HMA) or 60 μM (OsHPP10-HMA). This was titrated with
1004 AVR-Pia at a concentration 10X greater than that of the HMA domain (180 uM, 350 uM or 600
1005 uM). Each experiment consisted of a single injection of 0.5 μL followed by 18 injections of 2
1006 μL each at 150 s intervals with a stirring speed of 750 rpm. Data were processed with the
1007 MicroCal PEAQ-ITC analysis software (Malvern Panalytical). Experiments were carried out in
1008 triplicate.

1009 **Crystallisation of OsHPP09-HMA and AVR-Pia**

1010 Sitting drop, vapour diffusion crystallisation trials were set up in 96-well Swissci 3 lens
1011 crystallisation plates using dragonfly and mosquito dispensing robots (SPT Labtech). 100 nL
1012 of protein at a concentration of 8.6 mg/ml was combined with 100 nL reservoir solution.
1013 Needle-like crystals were observed in multiple conditions in the commercial Structure Screen
1014 1 + 2 (HT-96; Molecular Dimensions) and PEGs Suite (NeXtal) screens, however these were
1015 unsuitable for X-ray diffraction. Optimisation around these conditions yielded multiple crystals
1016 suitable for diffraction studies. The X-ray diffraction data used to solve the structure was
1017 obtained from a crystal harvested from the condition containing 0.1 M MES pH 6.5, 0.2 M
1018 ammonium sulphate, 20% (w/v) PEG 4000. The crystal was mounted in a nylon loop and flash-
1019 frozen in liquid nitrogen prior to shipping to the European Synchrotron Radiation Facility.

1020 **X-ray diffraction data collection and processing and model refinement**

1021 X-ray diffraction data were collected on beamline MASSIF-1 (ID30A-1) at the European
1022 Synchrotron Radiation Facility. Data were processed with the EDNA autoprocessing pipeline
1023 [78]. The scaled, unmerged data file was passed to AIMLESS for data reduction [79,80]
1024 (implemented in CCP4i2 [81]). The AVR-Pia/OsHPP09-HMA structure was solved by molecular
1025 replacement with PHASER [82], using a monomer of AVR-Pia (PDB accession 6Q76, chain B)
1026 and a monomer of OsHPP09-HMA (modelled with ColabFold [83]). Iterative cycles of manual
1027 adjustment, refinement, and validation were carried out using COOT [84], REFMAC5 [85,86] and
1028 MolProbity [87,88], implemented in CCP4i2. Analysis of the interface was performed with qtPISA
1029 [52]. Interatomic distances were measured and structure superposition/RMSD calculations were
1030 performed with PyMOL v2.5.0 Open-Source [89]. Structure figures were prepared using the
1031 CCP4 molecular graphics (CCP4mg) software [90].

1032 **Structural modelling of AVR-Pia/HMA complexes**

1033 Structural modelling of AVR-Pia/HMA complexes was carried out with both ColabFold v1.5.5
1034 ([83] (based on AlphaFold2 Multimer v3 [91,92]) and the AlphaFold3 web server
1035 (alphafoldserver.com; models generated between 2024-05-27 and 2024-07-02) [93]. For models
1036 generated with ColabFold, no template information from the PDB was used (template_mode:
1037 none) and the number of recycles was set to 20 (num_recycles: auto). Five models were
1038 generated for each complex and were relaxed using AMBER (num_relax: 5). Default settings
1039 were otherwise used. For models generated with AlphaFold3, default settings were used. At
1040 the time of use, AlphaFold3 did not support excluding template information from the PDB. Five
1041 models were generated for each complex using five different seed values. Interface analysis
1042 was carried out with qtPISA [52].

1043 ## Data availability

1044 The protein structure of the complex between OsHPP09-HMA and AVR-Pia has been
1045 deposited in the Protein Data Bank with accession number 9RSV (pdb_00009RSV). X-ray
1046 diffraction data are publicly available via the European Synchrotron Radiation Facility [94].

1047

1048 ## Figure Legends

1049 **Fig. 1. AVR-Pia interacts with OsH(I)PPs.**

1050 **a** Y2H interaction analysis between AVR-Pia (upper panel) or MAX58 (lower panel) and either
1051 the heavy metal-associated (HMA) domain or full-length (FL) proteins of OsH(I)PPs. The
1052 OsH(I)PP candidates were previously identified in a comprehensive pairwise Y2H analysis
1053 using AVR-Pia as prey and a library of HMA domains from OsH(I)PPs as bait. $OsRGA5_{Cter}$
1054 (883 – 1116 aa) was included as a positive control in the experiment with AVR-Pia/OsH(I)PPs
1055 (top panel). After an interaction was observed between OsHPP09 and AVR-Pia, this
1056 interaction was used as a positive control in the subsequent experiment with MAX58 (bottom
1057 panel).. Serial dilutions of diploid yeast were spotted onto synthetic defined (SD) media to
1058 monitor growth (SD/-LW) or to assess protein-protein interactions (SD/-LWH and SD/-LWH
1059 supplemented with 0.5 mM 3AT). Photos were taken after 7 days of incubation. Ø indicates
1060 positions where no yeast was spotted. AD, activating domain; BD, binding domain. **b**
1061 Quantitative measurement of luciferase-derived signals shows that AVR-Pia, but not MAX58,
1062 interacts with OsHPP09, OsHPP10, OsHPP11 and OsHIPP21 in a split-luciferase
1063 complementation assay. Neither AVR-Pia nor MAX58 interact with any other tested OsHIPP
1064 in planta. AVR-Pia and MAX58 were fused to the N-terminal part of luciferase
1065 (3xHA:NLuc:AVR-Pia, 3xHA:NLuc:MAX58) and co-expressed with OsH(I)PP FL proteins
1066 fused at their N-termini to the C-terminal part of luciferase (3xFlag:CLuc:OsH(I)PP). Co-
1067 expression of AVR-Pia with $OsRGA5_{Cter}$ (883 – 1116 aa) was used as a positive control.
1068 Leaves infiltrated with P19 alone served as background (BG) control. Leaf discs were collected
1069 2 days post infiltration. Box plots show the median (line), mean (cross) and upper/lower
1070 quartiles (box limits), whiskers extend to the most extreme data points within 1.5x the
1071 interquartile range. Values outside this range are shown as individual data points. Three
1072 independent replicates were performed (n = 8 per replicate). Due to experimental constraints,
1073 the following sample sizes apply to specific conditions: AVR-Pia/OsHPP09: n = 16 in replicates
1074 1 and 2. Data points are individually plotted and shaped according to the replicate. Different
1075 letters indicate statistically significant differences based on a pairwise Wilcoxon test ($\alpha = 0.05$).

1076 **Fig. 2. AVR-Pia-H3 does not interact with OsHPP09, OsHPP10, OsHPP11 and HIPP21.**

1077 **a** Y2H interaction analysis between AVR-Pia-H3 and either the heavy metal-associated (HMA)
1078 domain or full-length (FL) proteins of OsH(I)PPs. OsHPP09/AVR-Pia served as positive
1079 control. Serial dilutions of diploid yeast were spotted onto synthetic defined (SD) media to
1080 monitor growth (SD/-LW) or to assess protein-protein interactions (SD/-LWH). Photos were
1081 taken after 7 days of incubation. AD, activating domain; BD, binding domain. **b** Quantitative
1082 measurement of luciferase-derived signals shows that AVR-Pia-H3 does not interact with

1083 OsHPP09, OsHPP10, OsHPP11 and OsHIPP21 in a split-luciferase complementation assay.
1084 MAX effectors were fused to the N-terminal part of luciferase (3xHA:NLuc:MAX) and co-
1085 expressed with OsH(I)PP FL proteins fused at their N-termini to the C-terminal part of
1086 luciferase (3xFlag:CLuc:OsH(I)PP). Co-expression of AVR-Pia with OsHPP09 served as
1087 positive control, co-expression of OsHPP09/MAX58 and $OsRGA5_{Cter}$ (883 – 1116 aa)/AVR-
1088 Pia-H3 served as negative controls. Leaves infiltrated with P19 alone served as background
1089 (BG) control. Leaf discs were collected 2 days post infiltration. Box plots show the median
1090 (line), mean (cross) and upper/lower quartiles (box limits), whiskers extend to the most
1091 extreme data points within 1.5x the interquartile range. Values outside this range are shown
1092 as individual data points. Three independent replicates were performed, with n = 8 per
1093 combination per replicate. Due to experimental constraints, the following sample sizes apply
1094 to specific conditions: AVR-Pia/OsHPP09: n = 16 in replicates 1 and 2. Data points are
1095 individually plotted and shaped according to the replicate. Different letters indicate statistically
1096 significant differences based on a pairwise Wilcoxon test (α = 0.05). **c** Analytical gel filtration
1097 traces obtained from injection of OsHPP09-HMA alone (top panel), AVR-Pia-H3 alone (middle
1098 panel) and the two proteins in a 1:1 molar ratio (bottom panel). Significant peaks are indicated
1099 by coloured dashed lines with the elution volume labelled. SDS-PAGE gel inserts show
1100 fractions from peak elution volumes indicated by the grey shaded regions. OsHPP09-HMA
1101 absorbs light at 280 nm poorly (molar extinction coefficient of 1490 $M^{-1}cm^{-1}$) so the peak
1102 corresponding to OsHPP09-HMA is small. The elution volume observed for OsHPP09-HMA
1103 is consistent with dimerisation, as has been observed for other purified HMA domains
1104 [10,50]. There is no shift in the elution volume for AVR-Pia-H3 in the presence of OsHPP09-HMA
1105 indicating that the two proteins do not form a complex.

1106

1107 **Fig. 3. OsH(I)PPs interacting with AVR-Pia do not interact with AVR1-CO39.**

1108 **a** Y2H interaction analysis between AVR1-CO39 and either the heavy metal-associated
1109 (HMA) domain or full-length (FL) proteins of OsH(I)PPs. $OsRGA5_{Cter}$ (883 – 1116 aa)/AVR1-
1110 CO39 served as positive control. Serial dilutions of diploid yeast were spotted onto synthetic
1111 defined (SD) media to monitor growth (SD/-LW) or to assess protein-protein interactions (SD/-
1112 LWH). Photos were taken after 7 days of incubation. Ø indicates positions where no yeast was
1113 spotted. AD, activating domain; BD, binding domain. **b** Quantitative measurement of
1114 luciferase-derived signals shows that AVR1-CO39 does weakly interact with OsHPP09,
1115 OsHPP10 and OsHPP11 but not with OsHIPP21 in a split-luciferase complementation assay.
1116 MAX effectors were fused to the N-terminal part of luciferase (3xHA:NLuc:MAX) and co-
1117 expressed with OsH(I)PP FL proteins fused at their N-termini to the C-terminal part of
1118 luciferase (3xFlag:CLuc:OsH(I)PP). Co-expression of AVR-Pia or AVR1-CO39 with OsPi21

1119 served as negative controls, while AVR-Pia/OsHPP09 served as a positive control. Leaf discs
1120 were collected 2 days post infiltration. Box plots show the median (line), mean (cross) and
1121 upper/lower quartiles (box limits), whiskers extend to the most extreme data points within 1.5x
1122 the interquartile range. Values outside this range are shown as individual data points. Three
1123 independent replicates were performed, with n = 8 per combination per replicate. Data points
1124 are individually plotted and shaped according to the replicate. Different letters indicate
1125 statistically significant differences based on a pairwise Wilcoxon test ($\alpha = 0.05$). **c** Analytical
1126 gel filtration traces obtained from injection of OsHPP09-HMA alone (top panel), AVR1-CO39
1127 alone (middle panel) and the two proteins in a 1:1 molar ratio (bottom panel). Significant peaks
1128 are indicated by coloured dashed lines with the elution volume labelled. SDS-PAGE gel inserts
1129 show fractions from peak elution volumes indicated by the grey shaded regions. OsHPP09-
1130 HMA absorbs light at 280 nm poorly (molar extinction coefficient of 1490 $M^{-1}cm^{-1}$) so the peak
1131 corresponding to OsHPP09-HMA is small. The small peak at ~13.7 ml in the trace for AVR1-
1132 CO39 is likely due to some dimerisation of the AVR1-CO39 protein; the quantity of protein is
1133 insufficient to observe a corresponding band on the SDS-PAGE gel. The elution volume
1134 observed for OsHPP09-HMA is consistent with dimerisation, as has been observed for other
1135 purified HMA domains [10,50]. There is no shift in the elution volume for AVR1-CO39 in the
1136 presence of OsHPP09-HMA indicating that the two proteins do not form a complex.

1137

1138 **Fig. 4. OsH(I)PPs interacting with AVR-Pia do not interact with AVR-Pik or Pwl2.**

1139 **a** Y2H interaction analysis between AVR-PikC, AVR-PikD, Pwl2 and AVR-Pia and either the
1140 heavy metal-associated (HMA) domain or full-length (FL) proteins of OsH(I)PPs.
1141 OsHIPP19/AVR-PikC, OsHIPP20/AVR-PikC, OsHIPP19/AVR-PikD, OsHIPP20/AVR-PikD
1142 and OsHIPP43/Pwl2 served as positive controls. Serial dilutions of diploid yeast were spotted
1143 onto synthetic defined (SD) media to monitor growth (SD/-LW) or to assess protein-protein
1144 interactions (SD/-LWH). Photos were taken after 7 days of incubation. AD, activating domain;
1145 BD, binding domain. **b** Quantitative measurement of luciferase-derived signals shows that
1146 AVR-PikC and AVR-PikD do not interact with OsHPP09, OsHPP10, OsHPP11 and
1147 OsHIPP21, while Pwl2 shows weak luminescence signals with these proteins, suggesting
1148 weak interactions. AVR-Pia also interacts with OsHIPP19 and OsHIPP20 in planta. MAX
1149 effectors were fused to the N-terminal part of luciferase (3xHA:NLuc:MAX) and co-expressed
1150 with OsH(I)PP FL proteins fused at their N-termini to the C-terminal part of luciferase
1151 (3xFlag:CLuc:OsH(I)PP). Co-expression of AVR-PikC/AVR-PikD with OsHIPP19/20 and Pwl2
1152 with OsHIPP43 served as positive controls, AVR-Pia with OsHIPP43 served as negative
1153 control. Leaves infiltrated with P19 alone served as background (BG) control. Leaf discs were
1154 collected 2 days post infiltration. Box plots show the median (line), mean (cross) and

1155 upper/lower quartiles (box limits), whiskers extend to the most extreme data points within 1.5x
1156 the interquartile range. Values outside this range are shown as individual data points. Unless
1157 otherwise stated, three independent replicates were performed, with n = 8 per combination
1158 per replicate. Due to experimental constraints, the following sample sizes apply to specific
1159 conditions: AVR-Pia/OsHIPP19 and AVR-Pia/OsHIPP20 in AVR-PikC and AVR-PikD panels:
1160 n = 4 in replicates 1 and 3. BG control in AVR-PikC and AVR-PikD panels: n = 3 in replicates
1161 1 and 3 and BG control in Pwl2 panel: n = 2 in replicates 1 and 3. AVR-PikD/OsHIPP19 n =
1162 16 in replicates 1 and 3 and n = 24 in replicate 2. Data points are individually plotted and
1163 shaped according to the replicate. Different letters indicate statistically significant differences
1164 based on a pairwise Wilcoxon test (α = 0.05).

1165

1166 **Fig. 5. AVR-Pia binds the HMA domains of OsH(I)PPs with varying affinities.**

1167 **a** Representative ITC experiments for each of the AVR-Pia/HMA interactions tested. Top panel
1168 shows the raw thermogram obtained from titration of AVR-Pia into a solution containing the
1169 purified HMA domains. Central panel shows the integrated heats (coloured dots) and binding
1170 isotherm fitted to a single site model (black line) using the MicroCal PEAQ-ITC analysis
1171 software (Malvern Panalytical). Bottom panel shows the differences (coloured crosses)
1172 between the modelled and observed values (residuals). **b** Dot plot representation of the
1173 apparent KD for each of the AVR-Pia/HMA interactions in three independent experiments.
1174 Coloured dots represent the KD vales determined in each replicate with coloured lines
1175 representing the error associated with the KD value as determined by the MicroCal PEAQ-
1176 ITC analysis software (Malvern Panalytical).

1177

1178 **Fig. 6. Crystal structure of the HMA domain of OsHPP09 in complex with AVR-Pia.**

1179 The structures of OsHPP09-HMA and AVR-Pia are represented as teal and gold ribbons,
1180 respectively. The amino acids comprising β2 of AVR-Pia and β2 of the HMA domain are
1181 represented as cylinders. Side chains involved in intermolecular hydrogen bonds/salt bridges
1182 are also represented as cylinders. Hydrogen bonds are represented by black dashed lines
1183 labelled with the bond length. Left insert shows main chain hydrogen bonds between AVR-
1184 Pia-β2 and OsHPP09-β2. Right insert shows intermolecular contacts between side chains of
1185 residues in OsHPP09-α1 and AVR-Pia.

1186

1187 **Fig. 7. Mutation of OsHPP09 E16 reduces AVR-Pia binding.**

1188 **a** Y2H interaction analysis between AVR-Pia and full-length (FL) OsHPP09 mutant versions
1189 carrying single mutations in the binding interface. OsHPP09^{WT}/AVR-Pia served as positive
1190 control. Serial dilutions of diploid yeast were spotted onto synthetic defined (SD) media to
1191 monitor growth (SD/-LW) or to assess protein-protein interactions (SD/-LWH and SD/-LWH
1192 supplemented with 5 mM 3AT). Photos were taken after 7 days of incubation. AD, activating
1193 domain; BD, binding domain. **b** Quantitative measurement of luciferase-derived signals shows
1194 that the E16A, E16R and I35K mutations in OsHPP09 significantly reduce its interaction with
1195 AVR-Pia in a split-luciferase complementation assay. AVR-Pia was fused to the N-terminal
1196 part of luciferase (3xHA:NLuc:AVR-Pia) and co-expressed with OsH(I)PP FL proteins fused
1197 at their N-termini to the C-terminal part of luciferase (3xFlag:CLuc:OsH(I)PP). Co-expression
1198 of AVR-Pia with OsHPP09 served as positive control, co-expression of OsHIPP43 with AVR-
1199 Pia served as negative control. Leaves infiltrated with P19 alone served as background (BG)
1200 control. Leaf discs were collected 2 days post infiltration. Box plots show the median (line),
1201 mean (cross) and upper/lower quartiles (box limits), whiskers extend to the most extreme data
1202 points within 1.5x the interquartile range. Values outside this range are shown as individual
1203 data points. Three independent replicates were performed, with n = 8 per combination per
1204 replicate. Data points are individually plotted and shaped according to the replicate. Different
1205 letters indicate statistically significant differences based on a pairwise Wilcoxon test ($\alpha = 0.05$).
1206 **c** Circular dichroism (CD) spectra obtained for WT OsHPP09-HMA (pale blue) and variants
1207 carrying E16A, E16R, I35K or D33H mutations. Negative peaks at 222 nm and 208 nm and a
1208 positive peak at 193 nm are indicative of α-helices while a negative peak at 218 nm and
1209 positive peak at 195 nm are indicative of β-sheets, consistent with the expected βαββαβ
1210 topology of an HMA domain. In the case of the I35K mutant, low ellipticity above 210 nm and
1211 a negative peak at 200 nm is indicative of disorder. **d** Overlays of cross-peaks from HSQC
1212 spectra corresponding to residues L39, I44, E56 and Y85 of ^{15}N-labelled AVR-Pia alone
1213 (orange) and in the presence of either WT OsHPP09-HMA or variants carrying E16A, E16R
1214 or D33H mutations (blue/green/purple). Overlays of the full spectra are provided in Supp.
1215 Figures S19-S21. Chemical shift perturbation of ^{15}N-labelled AVR-Pia is indicative of an
1216 interaction with the HMA domain.

1217

1218 ## Supplementary Figure and Table Legends

1219 **Supplementary Fig. 1. AVR-Pia interacts with HMA domains from OsH(I)PPs.**

1220 Comprehensive pairwise Y2H analysis using AVR-Pia, MAX58, Pwl2, and AVR-PikD as prey,
1221 and a library of HMA domains from OsH(I)PPs as bait [47]. The left panel shows yeast growth
1222 on selective media, while the right panel identifies the rice H(I)PP proteins from which the
1223 HMA domains were derived. Diploid yeast were spotted onto synthetic defined (SD) media to
1224 monitor growth (SD/-LW) or to assess protein-protein interactions (SD/-LWH). Pictures were
1225 taken after 7 days of incubation. AD, activating domain; BD, binding domain; *, Autoactive BD
1226 construct leading to yeast growth regardless of the presence or identity of the AD construct;
1227 +++, strong yeast growth; ++, normal yeast growth, +, weak yeast growth; No HMA, proteins
1228 for which no HMA domain was identified by sequence analysis or structural prediction; Wrong
1229 annotation, constructs based on misannotated genes, resulting in missing or truncated HMA
1230 domains, thereby compromising Y2H assay.

1231 **Supplementary Fig. 2. Mutation of the isoprenylation motif of OsHIPPs does not**
1232 **promote AVR-Pia interaction.**

1233 Y2H interaction analysis between AVR-Pia and either wildtype (WT) full-length (FL) OsHIPPs,
1234 including OsHIPP14, OsHIPP21, OsHIPP39 and OsHIPP41, or the corresponding FL OsHIPP
1235 isoprenylation mutants, in which the cysteine (C) residue was replaced by a non-prenylatable
1236 serine (S) residue. OsHPP09/AVR-Pia and was included as positive control. Serial dilutions
1237 of diploid yeast were spotted onto synthetic defined (SD) media to monitor growth (SD/-LW)
1238 or to assess protein-protein interactions (SD/-LWH). Photos were taken after 7 days of
1239 incubation. AD, activating domain; BD, binding domain. OsHIPP$^{C/S}$ mutants: OsHIPP14^{C187S},
1240 OsHIPP21^{C133S}, OsHIPP39^{C190S}, OsHIPP41^{C152S}.

1241 **Supplementary Fig. 3. Expression of bait and prey proteins in haploid yeast.**

1242 **a** Total yeast protein extracts from haploid yeast were separated on a 10 – 20% Tricine SDS-
1243 PAGE gel and analysed by immunoblot using an anti-BD antibody to detect Gal4-BD fusion
1244 proteins with either the heavy metal-associated (HMA) domain, full-length (FL) OsH(I)PPs and
1245 the OsHIPP21 isoprenylation mutant (C/S). Protein loading is indicated by Ponceau S staining
1246 (PS). **b** Total yeast protein extracts from haploid yeast were separated on a 10% NuPAGE™
1247 Bis-Tris gel and analysed by immunoblot using an anti-BD antibody to detect Gal4-BD fusion
1248 proteins with either the HMA domain, FL OsHIPPs and their corresponding isoprenylation
1249 mutants (C/S). Protein loading is indicated by Ponceau S staining (PS). **c** Total yeast protein
1250 extracts from haploid yeast were separated on a NuPAGE™ Bis-Tris gel and analysed by
1251 immunoblot using an anti-HA antibody to detect Gal4-AD fusion proteins with MAX effectors.

1252 Protein loading is indicated by Ponceau S staining (PS). **d** Total yeast protein extracts from
1253 haploid yeast were separated on a 10% NuPAGE™ Bis-Tris gel and analysed by immunoblot
1254 using an anti-BD antibody to detect Gal4-BD fusion proteins with FL OsHPP09 wildtype (WT)
1255 and mutant versions. Protein loading is indicated by Ponceau S staining (PS). OsHIPP$^{C/S}$
1256 mutants: OsHIPP14^{C187S}, OsHIPP21^{C133S}, OsHIPP39^{C190S}, OsHIPP41^{C152S}.

1257 **Supplementary Fig. 4. Amino acid alignment of OsHPP09, OsHPP10, OsHPP11,**
1258 **OsHIPP21 and the C-terminus of OsRGA5.**

1259 Amino acid alignment of full-length OsHPP09, OsHPP10, OsHPP11 and OsHIPP21 and
1260 residues 995-1116 of OsRGA5, including the HMA domain and the C-terminal region of the
1261 protein which concludes with a putative CaaX isoprenylation motif (CSTM). Sequence
1262 alignment was carried out with Clustal Omega. The blue shaded box highlights the HMA
1263 domain, while the yellow shaded box highlights the CaaX motif present in OsHIPP21 and
1264 OsRGA5.

1265 **Supplementary Fig. 5. Expression of CLuc- and NLuc fusion proteins (related to Fig. 1).**

1266 Immunoblot analysis of transiently expressed proteins in *N. benthamiana*, including
1267 OsH(I)PPs N-terminally tagged with a 3xFlag epitope fused to the C-terminal part of luciferase
1268 (CLuc), and AVR-Pia and MAX58 N-terminally tagged with 3xHA and the N-terminal part of
1269 luciferase (NLuc). This experiment corresponds to replicate 1 of Fig. 1. Detection was
1270 performed using anti-Flag and anti-HA antibodies. Membrane was stripped after anti-Flag
1271 detection and re-probed with anti-HA. Protein loading is indicated by the Rubisco band
1272 visualized by Ponceau S. staining (PS).

1273 **Supplementary Fig. 6. AlphaFold2 models do not differentiate between HMA domains**
1274 **which interact with AVR-Pia and those which do not.**

1275 AlphaFold2 (ColabFold v1.5.5) models of AVR-Pia in complex with HMA domains which **a**
1276 were experimentally shown to interact with AVR-Pia and **b** do not interact with AVR-Pia.
1277 Structure models are represented as ribbons and coloured by pLDDT score using the classical
1278 AlphaFold colour scheme as shown in the key. **c** Plots of ipTM, pTM and Multimer (0.8*iPTM
1279 + 0.2*pTM) scores for each of the five models generated for each HMA/AVR-Pia complex.
1280 Points indicate scores of individual models; green and purple lines indicate mean values for
1281 AVR-Pia-interacting and non-interacting HMA domains, respectively. **d** Comparison of
1282 interface parameters determined by qtPISA [52]) for the top ranked model of each HMA/AVR-
1283 Pia complex. Green and purple points indicate values for individual HMA/AVR-Pia models.
1284 The centre line of the box represents the median and the limits of the box represent the upper

1285 and lower quartiles. Whiskers extend to the smallest value within (Q1 − 1.5 × the interquartile
1286 range (IQR)) and the largest value within (Q3 + 1.5 × IQR).

1287 **Supplementary Fig. 7. AlphaFold3 models do not clearly differentiate between HMA**
1288 **domains which interact with AVR-Pia and those which do not.**

1289 AlphaFold3 models of AVR-Pia in complex with HMA domains which **a** were experimentally
1290 shown to interact with AVR-Pia and **b** do not interact with AVR-Pia. Structure models are
1291 represented as ribbons and coloured by pLDDT score using the classical AlphaFold colour
1292 scheme as shown in the key. **c** Plots of ipTM, pTM and Multimer (0.8*iPTM + 0.2*pTM) scores
1293 for each of the top ranked models from each of the five seeds used to model each HMA/AVR-
1294 Pia complex. Points indicate scores of individual models; green and purple lines indicate mean
1295 values for AVR-Pia-interacting and non-interacting HMA domains, respectively. **d** Comparison
1296 of interface parameters determined by qtPISA [52]) for the top ranked model (selected from
1297 models from all five seeds) of each HMA/AVR-Pia complex. Green and purple points indicate
1298 values for individual HMA/AVR-Pia models. The centre line of the box represents the median
1299 and the limits of the box represent the upper and lower quartiles. Whiskers extend to the
1300 smallest value within (Q1 − 1.5 × the interquartile range (IQR)) and the largest value within
1301 (Q3 + 1.5 × IQR).

1302 **Supplementary Fig. 8. AVR-Pia H3 differs from AVR-Pia in two amino acid positions.**

1303 **a** Multiple sequence alignment of AVR-Pia variants from Magnaporthe oryzae isolates
1304 described in [6]. Signal peptide is highlighted by a shaded grey box. Polymorphic residues 24
1305 (F, S) and 46 (T, N) are indicated in a purple outlined box. Arrows above the alignment indicate
1306 secondary structure elements. **b** The polymorphic residues F24 and T46 are located at the
1307 HMA binding interface. Crystal structure of AVR-Pia in complex with Pikp-HMA (PDB 6Q76;
1308 [45]). AVR-Pia and Pikp-HMA are represented as gold and teal ribbons, respectively, with the
1309 side chains of AVR-Pia T46 and F24S shown in purple.

1310 **Supplementary Fig. 9. Expression of CLuc- and NLuc fusion proteins (related to Fig. 2).**

1311 Immunoblot analysis of transiently expressed proteins in *N. benthamiana*, including
1312 OsH(I)PPs and $OsRGA5_{Cter}$ (883 – 1116 aa) N-terminally tagged with a 3xFlag epitope fused
1313 to the C-terminal part of luciferase (CLuc), and AVR-Pia-H3 N-terminally tagged with 3xHA
1314 and the N-terminal part of luciferase (NLuc). This experiment corresponds to replicate 2 of Fig.
1315 5. Detection was performed using anti-Flag and anti-HA antibodies. Membrane was stripped
1316 after anti-Flag detection and re-probed with anti-HA. Protein loading is indicated by the
1317 Rubisco band visualized by Ponceau S. staining (PS).

1318 **Supplementary Fig. 10. AVR-Pia binds to the HMA domain of OsHPP09 in analytical size**
1319 **exclusion chromatography experiments.**

1320 Analytical gel filtration traces obtained from injection of OsHPP09-HMA alone (top panel),
1321 AVR-Pia alone (middle panel) and the two proteins in a 1:1 molar ratio (bottom panel).
1322 Significant peaks are indicated by dashed lines with the elution volume labelled. SDS-PAGE
1323 gel inserts show fractions from the peak elution volumes indicated by the grey shaded regions.
1324 OsHPP09-HMA absorbs light at 280 nm poorly (molar extinction coefficient of 1490 M-1cm-1)
1325 so the peak corresponding to OsHPP09-HMA is small. The elution volume observed for
1326 OsHPP09-HMA is consistent with dimerisation, as has been observed for other purified HMA
1327 domains [10,50]. The shift in the elution volume for AVR-Pia in the presence of OsHPP09-HMA
1328 indicates that the two proteins form a complex.

1329 **Supplementary Fig. 11. Expression of CLuc- and NLuc fusion proteins (related to Fig.**
1330 **3).**

1331 Immunoblot analysis of transiently expressed proteins in *N. benthamiana*, including
1332 OsH(I)PPs and $OsRGA5_{Cter}$ (883 – 1116 aa) N-terminally tagged with a 3xFlag epitope fused
1333 to the C-terminal part of luciferase (CLuc), and AVR1-CO39 N-terminally tagged with 3xHA
1334 and the N-terminal part of luciferase (NLuc). This experiment corresponds to replicate 1 of Fig.
1335 4. Detection was performed using anti-Flag and anti-HA antibodies. Membrane was stripped
1336 after anti-Flag detection and re-probed with anti-HA. Protein loading is indicated by the
1337 Rubisco band visualized by Ponceau S. staining (PS).

1338 **Supplementary Fig. 12. Expression of CLuc- and NLuc fusion proteins (related to Fig.**
1339 **4).**

1340 Immunoblot analysis of transiently expressed proteins in *N. benthamiana*, including
1341 OsH(I)PPs N-terminally tagged with a 3xFlag epitope fused to the C-terminal part of luciferase
1342 (CLuc), and AVR-Pia, AVR-PikC, AVR-PikD and Pwl2 N-terminally tagged with 3xHA and the
1343 N-terminal part of luciferase (NLuc). This experiment corresponds to replicate 1 of Fig. 2.
1344 Detection was performed using anti-Flag and anti-HA antibodies. Membrane was stripped
1345 after anti-Flag detection and re-probed with anti-HA. Protein loading is indicated by the
1346 Rubisco band visualized by Ponceau S. staining (PS).

1347 **Supplementary Fig. 13. Production and purification of OsHPP09-HMA.**

1348 **a** Size exclusion chromatography elution trace for 6xHis-MBP-OsHPP09-HMA (following the
1349 initial IMAC purification step). The SDS-PAGE gel shows fractions corresponding to the peak
1350 in the shaded area. **b** SDS-PAGE gel of pooled fractions following size exclusion
1351 chromatography before and after cleavage of the 6xHis-MBP tag with GST-tagged 3C

1352 protease. **c** SDS-PAGE gel showing flow-through, wash and elution fractions from tandem
1353 HisTrapTM, MBPTrapTM and GSTrapTM affinity columns. **d** Size exclusion chromatography
1354 elution trace for OsHPP09-HMA. OsHPP09-HMA absorbs light at 280nm poorly (molar
1355 extinction coefficient of 1490 $M^{-1}cm^{-1}$). The SDS-PAGE gel shows fractions corresponding to
1356 the three peaks in the shaded areas. The peak elution volume of OsHPP09-HMA (193.9 ml)
1357 is consistent with dimerisation of the HMA domain.

1358 **Supplementary Fig. 14. Replicates of the ITC experiments presented in Fig. 5.**

1359 Top panels show the raw thermograms obtained from titration of AVR-Pia into a solution
1360 containing the purified HMA domains. Central panels show the integrated heats (coloured
1361 dots) and binding isotherms fitted to a single site model (black line) using the MicroCal PEAQ-
1362 ITC analysis software (Malvern Panalytical). Bottom panels show the differences (coloured
1363 crosses) between the modelled and observed values (residuals).

1364 **Supplementary Fig. 15. Thermodynamic profiles from ITC experiments presented in**
1365 **Fig. 5 and Supp. Fig. S14.**

1366 Bars represent the magnitude of the determined thermodynamic parameters ΔG (blue bar),
1367 ΔH (green bar) and -TΔS (red bar).

1368 **Supplementary Fig. 16. Comparison of binding interfaces in the crystal structures of**
1369 **AVR-Pia in complex with OsHPP09-HMA (PDB accession code 9RSV), AVR-Pia/Pikp-**
1370 **HMA (6Q76, [45]) and AVR1-CO39/RGA5-HMA (5ZNG,[10])**

1371 **a** Global interface of the effector/HMA complex. Structures are represented as gold (AVR-
1372 Pia), teal (OsHPP09-HMA), brown (AVR-Pia), pale blue (Pikp-HMA), orange (AVR1-CO39)
1373 and green (RGA5-HMA) ribbons with relevant secondary structure elements indicated. **b**
1374 Hydrogen bonds between residues in β2 of the effector and β2 of the HMA domain. Main chain
1375 atoms are represented as cylinders (side chains not shown for clarity). Hydrogen bonds are
1376 represented as black dashed lines with lengths (determined by qtPISA) indicated. **c-f**
1377 Comparison of residues involved in forming intermolecular contacts at the effector/HMA
1378 interface. Structures are presented in ribbon representation with relevant residues shown as
1379 cylinders. Hydrogen bonds are represented as black dashed lines with lengths (determined
1380 by qtPISA) indicated. Water molecules are represented as red spheres.

1381 **Supplementary Fig. 17. HSQC spectra of 15N-AVR-Pia (40 μM) in the absence (orange**
1382 **cross-peaks) and presence (purple cross-peaks) of unlabelled OsHPP09-HMA (40 μM).**

1383 Cross-peak labels correspond to the ^{15}N-AVR-Pia spectra (previously assigned by [11]). Zoom
1384 inset panels show cross-peaks corresponding to residues L39, I44, E56 and Y85 to illustrate

1385 the chemical shift perturbations between the free (^{15}N-AVR-Pia alone) and bound (^{15}N-AVR-
1386 Pia with OsHPP09-HMA). Zoomed areas are indicated by boxes on the spectra.

1387 **Supplementary Fig. 18. Expression of CLuc- and NLuc fusion proteins (related to Fig.**
1388 **7).**

1389 Immunoblot analysis of transiently expressed proteins in *N. benthamiana*, including OsHPP09
1390 wildtype (WT) and mutant versions N-terminally tagged with a 3xFlag epitope fused to the C-
1391 terminal part of luciferase (CLuc), and AVR-Pia N-terminally tagged with 3xHA and the N-
1392 terminal part of luciferase (NLuc). This experiment corresponds to replicate 2 of Fig. 7.
1393 Detection was performed using anti-Flag and anti-HA antibodies. Membrane was stripped
1394 after anti-Flag detection and re-probed with anti-HA. Protein loading is indicated by the
1395 Rubisco band visualized by Ponceau S. staining (PS). Dashed lines between bands indicate
1396 that lanes were cut from the same blot but were non-adjacent.

1397 **Supplementary Fig. 19. HSQC spectra of ^{15}N-AVR-Pia (40 µM) in the absence (orange**
1398 **cross-peaks) and presence (turquoise cross-peaks) of unlabelled OsHPP09^{D33H}-HMA**
1399 **(40 µM).**

1400 Cross-peak labels correspond to the ^{15}N-AVR-Pia spectra (previously assigned [11]). Zoom inset
1401 panels show cross-peaks corresponding to residues L39, I44, E56 and Y85 to illustrate the
1402 chemical shift perturbations between the free (^{15}N-AVR-Pia alone) and bound (^{15}N-AVR-Pia
1403 with OsHPP09^{D33H}-HMA) as presented in Fig. 7. Zoomed areas are indicated by boxes on the
1404 spectra.

1405 **Supplementary Fig. 20. HSQC spectra of ^{15}N-AVR-Pia (40 µM) in the absence (orange**
1406 **cross-peaks) and presence (blue cross-peaks) of unlabelled OsHPP09^{E16A}-HMA (40 µM).**

1407 Cross-peak labels correspond to the ^{15}N-AVR-Pia spectra (previously assigned [11]). Zoom inset
1408 panels show cross-peaks corresponding to residues L39, I44, E56 and Y85 to illustrate the
1409 chemical shift perturbations between the free (^{15}N-AVR-Pia alone) and bound (^{15}N-AVR-Pia
1410 with OsHPP09^{E16A}-HMA) as presented in Fig. 7. Zoomed areas are indicated by boxes on the
1411 spectra.

1412 **Supplementary Fig. 21. HSQC spectra of ^{15}N-AVR-Pia (40 µM) in the absence (orange**
1413 **cross-peaks) and presence (pale blue cross-peaks) of unlabelled OsHPP09^{E16R}-HMA (40**
1414 **µM).**

1415 Cross-peak labels correspond to the ^{15}N-AVR-Pia spectra (previously assigned [11]). Zoom inset
1416 panels show cross-peaks corresponding to residues L39, I44, E56 and Y85 to illustrate the
1417 chemical shift perturbations between the free (^{15}N-AVR-Pia alone) and bound (^{15}N-AVR-Pia

1418 with OsHPP09^{E16R}-HMA) as presented in Fig. 7. Zoomed areas are indicated by boxes on the
1419 spectra.

1420 **Supplementary Fig. 22. Comparison of binding interfaces in the crystal structures of**
1421 **MAX effectors bound to HMA domains of H(I)PPs.**

1422 The structures of AVR-Pia in complex with OsHPP09-HMA (PDB accession code 9RSV),
1423 AVR-PikF in complex with OsHIPP19-HMA (PDB accession code 7B1I [41]) and Pwl2 in
1424 complex with OsHIPP43-HMA (PDB accession code 8R7A [46]) are represented as gold (AVR-
1425 Pia), teal (OsHPP09-HMA), brown (Pwl2), green (OsHIPP43-HMA), pink (AVR-PikF) and grey
1426 (OsHIPP19-HMA) ribbons with relevant secondary structure elements indicated.
1427 Superposition of MAX effectors (left) and HMA domains (right) was carried out in CCP4mg
1428 using secondary structure matching.

1429 **Supplementary Table S1. Amino acid sequences and MSU/RGAP and RAP-DB/IRGSP**
1430 **identifiers for the H(I)PPs used in the present study.**

1431 **Supplementary Table S2. Rice proteins interacting with AVR-Pia in the Y2H screen.**

1432 Results of a Y2H screen using BD:AVR-Pia as bait and a cDNA library from the rice cultivar
1433 CO39. The number of positive clones with insert sequences (cloned in frame with Gal4 AD)
1434 corresponding to the designated proteins are shown. * Potential false positives found in >50%
1435 of the Y2H screens performed in the lab using various bait proteins.

1436 **Supplementary Table S3. Thermodynamic parameters obtained from ITC experiments.**

1437 **Supplementary Table S4. X-ray data collection and refinement statistics for OsHPP09-**
1438 **HMA / AVR-Pia**

1439 **Supplementary Table S5. Comparison of the binding interfaces of complexes between**
1440 **HMA domains and MAX effectors.**

1441 **Supplementary Table S6. List of primers used in this study.**

1442 **Supplementary Table S7. List of constructs generated in this study.**

1443

1444 ## References

1445 1. Baudin, M. *et al.* Pyricularia oryzae: Lab star and field scourge. *Mol Plant Pathol* **25**,
1446 (2024).

1447 2. Savary, S. *et al.* The global burden of pathogens and pests on major food crops. *Nat*
1448 *Ecol Evol* **3**, 430–439 (2019).

1449 3. Oliveira-Garcia, E., Yan, X., Oses-Ruiz, M., de Paula, S. & Talbot, N. J. Effector-
1450 triggered susceptibility by the rice blast fungus Magnaporthe oryzae. *New Phytologist*
1451 **241**, 1007–1020 (2024).

1452 4. de Guillen, K. *et al.* Structure analysis uncovers a highly diverse but structurally
1453 conserved effector family in phytopathogenic fungi. *PLoS Pathog* **11**, (2015).

1454 5. Lahfa, M. *et al.* The structural landscape and diversity of Pyricularia oryzae MAX
1455 effectors revisited. *PLoS Pathog* **20**, e1012176 (2024).

1456 6. Le Naour--Vernet, M. *et al.* Adaptive evolution in virulence effectors of the rice blast
1457 fungus Pyricularia oryzae. *PLoS Pathog* **19**, e1011294 (2023).

1458 7. Le Naour--Vernet, M. *et al.* Structure-guided insights into the biology of fungal effectors.
1459 *New Phytologist* **246**, 1460–1477 (2025).

1460 8. Liao, J. *et al.* Pathogen effectors and plant immunity determine specialization of the
1461 blast fungus to rice subspecies. *Elife* **5**, (2016).

1462 9. Cesari, S. *et al.* The rice resistance protein pair RGA4/RGA5 recognizes the
1463 Magnaporthe oryzae effectors AVR-Pia and AVR1-CO39 by direct binding. *Plant Cell*
1464 **25**, 1463–1481 (2013).

1465 10. Guo, L. *et al.* Specific recognition of two MAX effectors by integrated HMA domains in
1466 plant immune receptors involves distinct binding surfaces. *Proc Natl Acad Sci U S A*
1467 **115**, 11637–11642 (2018).

1468 11. Ortiz, D. *et al.* Recognition of the Magnaporthe oryzae effector AVR-Pia by the decoy
1469 domain of the rice NLR immune receptor RGA5. *Plant Cell* **29**, 156–168 (2017).

1470 12. Cesari, S. Multiple strategies for pathogen perception by plant immune receptors. *New*
1471 *Phytologist* vol. 219 17–24 Preprint at https://doi.org/10.1111/nph.14877 (2018).

1472 13. Cesari, S., Bernoux, M., Moncuquet, P., Kroj, T. & Dodds, P. N. A novel conserved
1473 mechanism for plant NLR protein pairs: The 'integrated decoy' hypothesis. *Front Plant*
1474 *Sci* **5**, (2014).

1475 14. Kroj, T., Chanclud, E., Michel-Romiti, C., Grand, X. & Morel, J. B. Integration of decoy
1476 domains derived from protein targets of pathogen effectors into plant immune receptors
1477 is widespread. *New Phytologist* **210**, 618–626 (2016).

1478 15. Sarris, P. F., Cevik, V., Dagdas, G., Jones, J. D. G. & Krasileva, K. V. Comparative
1479 analysis of plant immune receptor architectures uncovers host proteins likely targeted
1480 by pathogens. *BMC Biol* **14**, 1–19 (2016).

1481 16. Bailey, P. C. *et al.* Dominant integration locus drives continuous diversification of plant
1482 immune receptors with exogenous domain fusions. *Genome Biol* **19**, 1–18 (2018).

1483 17. Oikawa, K. *et al.* The blast pathogen effector AVR-Pik binds and stabilizes rice heavy
1484 metal-associated (HMA) proteins to co-opt their function in immunity. *PLoS Pathog* **20**,
1485 e1012647 (2024).

1486 18. Dykema, P. E. *et al.* A new class of proteins capable of binding transition metals. *Plant*
1487 *Mol Biol* **41**, 139–150 (1999).

1488 19. Suzuki, N., Yamaguchi, Y., Koizumi, N. & Sano, H. Functional characterization of a
1489 heavy metal binding protein Cdl19 from Arabidopsis. *Plant Journal* **32**, 165–173 (2002).

1490 20. De Abreu-Neto, J. B., Turchetto-Zolet, A. C., De Oliveira, L. F. V., Bodanese Zanettini,
1491 M. H. & Margis-Pinheiro, M. Heavy metal-associated isoprenylated plant protein (HIPP):
1492 characterization of a family of proteins exclusive to plants. *FEBS J* **280**, 1604–1616
1493 (2013).

1494 21. Tehseen, M., Cairns, N., Sherson, S. & Cobbett, C. S. Metallochaperone-like genes in
1495 Arabidopsis thaliana. *Metallomics* **2**, 556–564 (2010).

1496 22. Crowell, D. N. & Huizinga, D. H. Protein isoprenylation: the fat of the matter. *Trends*
1497 *Plant Sci* **14**, 163–170 (2009).

1498 23. Kay, B. K., Williamson, M. P. & Sudol, M. The importance of being proline: the
1499 interaction of proline-rich motifs in signaling proteins with their cognate domains. *The*
1500 *FASEB Journal* **14**, 231–241 (2000).

1501 24. Khan, I. U. *et al.* Identification of novel rice (Oryza sativa) HPP and HIPP genes tolerant
1502 to heavy metal toxicity. *Ecotoxicol Environ Saf* **175**, 8–18 (2019).

1503 25. Li, J. *et al.* Heavy metal stress-associated proteins in rice and Arabidopsis: genome-
1504 wide identification, phylogenetics, duplication, and expression profiles analysis. *Front*
1505 *Genet* **11**, (2020).

1506 26. Barr, Z. K., Werner, T. & Tilsner, J. Heavy Metal-Associated Isoprenylated Plant
1507 Proteins (HIPPs) at plasmodesmata: Exploring the link between localization and
1508 function. *Plants* vol. 12 Preprint at https://doi.org/10.3390/plants12163015 (2023).

1509 27. Barth, O., Vogt, S., Uhlemann, R., Zschiesche, W. & Humbeck, K. Stress induced and
1510 nuclear localized HIPP26 from Arabidopsis thaliana interacts via its heavy metal
1511 associated domain with the drought stress related zinc finger transcription factor
1512 ATHB29. *Plant Mol Biol* **69**, 213–226 (2009).

1513 28. Barth, O., Zschiesche, W., Siersleben, S. & Humbeck, K. Isolation of a novel barley
1514 cDNA encoding a nuclear protein involved in stress response and leaf senescence.
1515 *Physiol Plant* **121**, 282–293 (2004).

1516 29. Cowan, G. H. *et al.* Potato mop-top virus co-opts the stress sensor HIPP26 for long-
1517 distance movement. *Plant Physiol* **176**, 2052–2070 (2018).

1518 30. Radakovic, Z. S. *et al.* Arabidopsis HIPP27 is a host susceptibility gene for the beet
1519 cyst nematode Heterodera schachtii. *Mol Plant Pathol* **19**, 1917–1928 (2018).

1520 31. Fukuoka, S. *et al.* Loss of function of a proline-containing protein confers durable
1521 disease resistance in Rice. *Science (1979)* **325**, 998–1001 (2009).

1522 32. Were, V. M. *et al.* The Magnaporthe oryzae effector Pwl2 alters HIPP43 localization to
1523 suppress host immunity. *Plant Cell* (2025) doi:10.1093/PLCELL/KOAF116.

1524 33. Huang, Z. *et al.* Small secreted effector protein from Fusarium sacchari suppresses
1525 host immune response by inhibiting ScPi21-induced cell death. *Mol Plant Pathol* **25**,
1526 e13414 (2024).

1527 34. Song, H. *et al.* The Meloidogyne graminicola effector MgMO289 targets a novel copper
1528 metallochaperone to suppress immunity in rice. *J Exp Bot* **72**, 5638–5655 (2021).

1529 35. Huang, Q. *et al.* CRISPR/Cas9-mediated mutagenesis of the susceptibility gene
1530 OsHPP04 in rice confers enhanced resistance to rice root-knot nematode. *Front Plant*
1531 *Sci* **14**, (2023).

1532 36. Niu, X. *et al.* A small secreted protein, RsMf8HN, in Rhizoctonia solani triggers plant
1533 immune response, which interacts with rice OsHIPP28. *Microbiol Res* **266**, 127219
1534 (2023).

1535 37. Zhang, X. *et al.* Isolation and characterisation of cDNA encoding a wheat heavy metal-
1536 associated isoprenylated protein involved in stress responses. *Plant Biol* **17**, 1176–
1537 1186 (2015).

1538 38. Huang, G. *et al.* Genome-wide characterization of heavy metal-associated
1539 isoprenylated plant protein gene family from Citrus sinensis in response to
1540 huanglongbing. *Front Plant Sci* **15**, (2024).

1541 39. Imran, Q. M. *et al.* Nitric oxide responsive heavy metal-associated gene AtHMAD1
1542 contributes to development and disease resistance in Arabidopsis thaliana. *Front Plant*
1543 *Sci* **7**, 232346 (2016).

1544 40. Bentham, A. R. *et al.* A single amino acid polymorphism in a conserved effector of the
1545 multihost blast fungus pathogen expands host-target binding spectrum. *PLoS Pathog*
1546 **17**, e1009957- (2021).

1547 41. Maidment, J. H. R. *et al.* Multiple variants of the fungal effector AVR-Pik bind the HMA
1548 domain of the rice protein OsHIPP19, providing a foundation to engineer plant defense.
1549 *Journal of Biological Chemistry* **296**, (2021).

1550 42. Ashikawa, I. *et al.* Two adjacent nucleotide-binding site-leucine-rich repeat class genes
1551 are required to confer Pikm-specific rice blast resistance. *Genetics* **180**, 2267–2276
1552 (2008).

1553 43. Zdrzałek, R., Kamoun, S., Terauchi, R., Saitoh, H. & Banfield, M. J. The rice NLR pair
1554 Pikp-1/Pikp-2 initiates cell death through receptor cooperation rather than negative
1555 regulation. *PLoS One* **15**, (2020).

1556 44. Cesari, S. *et al.* New recognition specificity in a plant immune receptor by molecular
1557 engineering of its integrated domain. *Nat Commun* **13**, (2022).

1558 45. Varden, F. A. *et al.* Cross-reactivity of a rice NLR immune receptor to distinct effectors
1559 from the rice blast pathogen Magnaporthe oryzae provides partial disease resistance.
1560 *J Biol Chem* **294**, 13006–13016 (2019).

1561 46. Zdrzałek, R. *et al.* Bioengineering a plant NLR immune receptor with a robust binding
1562 interface toward a conserved fungal pathogen effector. *Proc Natl Acad Sci U S A* **121**,
1563 e2402872121 (2024).

1564 47. Langner, T., Kellner, R., Harant, A., Terauchi, R. & Kamoun, S. A clone resource of
1565 cereal heavy-metal associated (HMA) domains— putative targets of plant pathogen
1566 effector proteins. Preprint at https://doi.org/10.5281/zenodo.5148558 (2021).

1567 48. Gómez De La Cruz, D., Zdrzałek, R., Banfield, M. J., Talbot, N. J. & Moscou, M. J.
1568 Molecular mimicry of a pathogen virulence target by a plant immune receptor. *bioRxiv*
1569 (2024) doi:10.1101/2024.07.26.605320.

1570 49. Homma, F., Huang, J. & van der Hoorn, R. A. L. AlphaFold-Multimer predicts cross-
1571 kingdom interactions at the plant-pathogen interface. *Nat Commun* **14**, 6040 (2023).

1572 50. Maqbool, A. *et al.* Structural basis of pathogen recognition by an integrated HMA
1573 domain in a plant NLR immune receptor. *Elife* **4**, e08709 (2015).

1574 51. Ose, T. *et al.* Solution structure of an avirulence protein, AVR-Pia, from Magnaporthe
1575 oryzae. *J Biomol NMR* **63**, 229–235 (2015).

1576 52. Krissinel, E. & Henrick, K. Inference of macromolecular assemblies from crystalline
1577 state. *J Mol Biol* **372**, 774–797 (2007).

1578 53. Schymkowitz, J. *et al.* The FoldX web server: an online force field. *Nucleic Acids Res*
1579 **33**, W382–W388 (2005).

1580 54. Park, C. H. *et al.* The Magnaporthe oryzae effector AvrPiz-t targets the RING E3
1581 ubiquitin ligase APIP6 to suppress pathogen-associated molecular pattern–triggered
1582 immunity in rice. *Plant Cell* **24**, 4748–4762 (2012).

1583 55. Park, C. H. *et al.* The E3 ligase APIP10 connects the effector AvrPiz-t to the NLR
1584 receptor Piz-t in rice. *PLoS Pathog* **12**, (2016).

1585 56. Shi, X. *et al.* The fungal pathogen Magnaporthe oryzae suppresses innate immunity by
1586 modulating a host potassium channel. *PLoS Pathog* **14**, e1006878 (2018).

1587 57. Wang, R. *et al.* Immunity to rice blast disease by suppression of effector-triggered
1588 necrosis. *Current Biology* **26**, 2399–2411 (2016).

1589 58. Tang, M. *et al.* The Nup98 homolog APIP12 targeted by the effector AvrPiz-t is involved
1590 in rice basal resistance against Magnaporthe oryzae. *Rice* **10**, 1–11 (2017).

1591 59. Couch, B. C. *et al.* Origins of host-specific populations of the blast pathogen
1592 Magnaporthe oryzae in crop domestication with subsequent expansion of pandemic
1593 clones on rice and weeds of rice. *Genetics* **170**, 613–630 (2005).

1594 60. Tosa, Y. *et al.* Evolution of an avirulence gene, AVR1-CO39, concomitant with the
1595 evolution and differentiation of Magnaporthe oryzae. *Molecular Plant-Microbe*
1596 *Interactions* **18**, 1148–1160 (2005).

1597 61. Hála, M., Žárský, V., Swiezewska, E. & Surmacz, L. Protein prenylation in plant stress
1598 responses. *Molecules 2019, Vol. 24, Page 3906* **24**, 3906 (2019).

1599 62. Guo, T. *et al.* Arabidopsis HIPP proteins regulate endoplasmic reticulum-associated
1600 degradation of CKX proteins and cytokinin responses. *Mol Plant* **14**, 1918–1934 (2021).

1601 63. Nawaz, G. *et al.* Knockout of Pi21 by CRISPR/Cas9 and iTRAQ-based proteomic
1602 analysis of mutants revealed new insights into M. oryzae resistance in elite rice line.
1603 *Genes (Basel)* **11**, 1–24 (2020).

1604 64. Tao, H. *et al.* Engineering broad-spectrum disease-resistant rice by editing multiple
1605 susceptibility genes. *J Integr Plant Biol* **63**, 1639–1648 (2021).

1606 65. Zhou, Y. *et al.* Engineering of rice varieties with enhanced resistances to both blast and
1607 bacterial blight diseases via CRISPR/Cas9. *Plant Biotechnol J* **20**, 876–885 (2022).

1608 66. Hanika, K. *et al.* Impairment of tomato WAT1 enhances resistance to vascular wilt fungi
1609 despite severe growth defects. *Front Plant Sci* **12**, 721674 (2021).

1610 67. Kieu, N. P., Lenman, M., Wang, E. S., Petersen, B. L. & Andreasson, E. Mutations
1611 introduced in susceptibility genes through CRISPR/Cas9 genome editing confer
1612 increased late blight resistance in potatoes. *Sci Rep* **11**, 1–12 (2021).

1613 68. Wolter, M., Hollricher, K., Salamini, F. & Schulze-Lefert, P. The mlo resistance alleles
1614 to powdery mildew infection in barley trigger a developmentally controlled defence
1615 mimic phenotype. *MGG Molecular & General Genetics* **239**, 122–128 (1993).

1616 69. Kusch, S. *et al.* Arabidopsis mlo3 mutant plants exhibit spontaneous callose deposition
1617 and signs of early leaf senescence. *Plant Mol Biol* **101**, 21–40 (2019).

1618 70. Garcia-Ruiz, H., Szurek, B. & Van den Ackerveken, G. Stop helping pathogens:
1619 engineering plant susceptibility genes for durable resistance. *Curr Opin Biotechnol* **70**,
1620 187–195 (2021).

1621 71. Weber, E., Engler, C., Gruetzner, R., Werner, S. & Marillonnet, S. A modular cloning
1622 system for standardized assembly of multigene constructs. *PLoS One* **6**, e16765
1623 (2011).

1624 72. Engler, C., Kandzia, R. & Marillonnet, S. A one pot, one step, precision cloning method
1625 with high throughput capability. *PLoS One* **3**, (2008).

1626 73. Bentham, A. R. *et al.* pOPIN-GG: A resource for modular assembly in protein
1627 expression vectors. *bioRxiv* 2021.08.10.455798 (2021)
1628 doi:10.1101/2021.08.10.455798.

1629 74. Bernoux, M. *et al.* Structural and functional analysis of a plant resistance protein TIR
1630 domain reveals interfaces for self-association, signaling, and autoregulation. *Cell Host*
1631 *Microbe* **9**, 200–211 (2011).

1632 75. Kushnirov, V. V. Rapid and reliable protein extraction from yeast. *Yeast* **16**, 857–860
1633 (2000).

1634 76. Wishart, D. S. *et al.* 1H, 13C and 15N chemical shift referencing in biomolecular NMR.
1635 *J Biomol NMR* **6**, 135–140 (1995).

1636 77. Vranken, W. F. *et al.* The CCPN data model for NMR spectroscopy: Development of a
1637 software pipeline. *Proteins: Structure, Function and Genetics* **59**, 687–696 (2005).

1638 78. Incardona, M. F. *et al.* EDNA: A framework for plugin-based applications applied to X-
1639 ray experiment online data analysis. *J Synchrotron Radiat* **16**, 872–879 (2009).

1640 79. Evans, P. R. An introduction to data reduction: space-group determination, scaling and
1641 intensity statistics. *Acta Crystallogr D Biol Crystallogr* **67**, 282 (2011).

1642 80. Evans, P. R. & Murshudov, G. N. How good are my data and what is the resolution?
1643 *urn:issn:0907-4449* **69**, 1204–1214 (2013).

1644 81. Agirre, J. *et al.* The CCP4 suite: integrative software for macromolecular
1645 crystallography. *urn:issn:2059-7983* **79**, 449–461 (2023).

1646 82. McCoy, A. J. *et al.* Phaser crystallographic software. *urn:issn:0021-8898* **40**, 658–674
1647 (2007).

1648 83. Mirdita, M. *et al.* ColabFold: making protein folding accessible to all. *Nat Methods* **19**,
1649 679–682 (2022).

1650 84. Emsley, P., Lohkamp, B., Scott, W. G. & Cowtan, K. Features and development of Coot.
1651 *Acta Crystallogr D Biol Crystallogr* **66**, 486–501 (2010).

1652 85. Murshudov, G. N., Vagin, A. A. & Dodson, E. J. Refinement of macromolecular
1653 structures by the maximum-likelihood method. *Acta Crystallogr D Biol Crystallogr* **53**,
1654 240–255 (1997).

1655 86. Murshudov, G. N. *et al.* REFMAC5 for the refinement of macromolecular crystal
1656 structures. *urn:issn:0907-4449* **67**, 355–367 (2011).

1657 87. Davis, I. W., Murray, L. W., Richardson, J. S. & Richardson, D. C. MolProbity: Structure
1658 validation and all-atom contact analysis for nucleic acids and their complexes. *Nucleic*
1659 *Acids Res* **32**, (2004).

1660 88. Chen, V. B. *et al.* MolProbity: All-atom structure validation for macromolecular
1661 crystallography. *Acta Crystallogr D Biol Crystallogr* **66**, 12–21 (2010).

1662 89. Schrödinger LLC. *The PyMOL Molecular Graphics System, Version 2.5.0 Open-*
1663 *Source*. (2015).

1664 90. McNicholas, S., Potterton, E., Wilson, K. S. & Noble, M. E. M. Presenting your
1665 structures: the CCP4mg molecular-graphics software. *urn:issn:0907-4449* **67**, 386–394
1666 (2011).

1667 91. Evans, R. *et al.* Protein complex prediction with AlphaFold-Multimer. *bioRxiv* (2022)
1668 doi:10.1101/2021.10.04.463034.

1669 92. Jumper, J. *et al.* Highly accurate protein structure prediction with AlphaFold. *Nature*
1670 **596**, 583–589 (2021).

1671 93. Abramson, J. *et al.* Accurate structure prediction of biomolecular interactions with
1672 AlphaFold 3. *Nature* **630**, 493–500 (2024).

94. Maidment, J. H. R., Bocquet, A., Gelin, M., De Guillen, K. & Cesari, S. BAG Montpellier [Dataset]. Preprint at https://doi.org/10.15151/ESRF-DC-2199982133 (2025).

Acknowledgements

We thank Mark Youles (The Sainsbury Laboratory, Norwich, UK) and Mark Banfield (John Innes Centre, Norwich UK) for generating and providing the pOPIN-GG vector and tag modules. Gateway-compatible split-luciferase vectors were kindly provided by Laurent Deslandes (INRAE Toulouse, France). We also thank Florian Veillet (Plant Health Institute of Montpellier, France) for providing the pFV79 construct used in this study. We are grateful to Julie Noell (Centre de Biologie Structurale, France) for assistance with protein purification, and to Corinne Lionne and Manon Mallet (Centre de Biologie Structurale, France) for helpful discussions about isothermal titration calorimetry methods. We thank Sebastien Ribeiro (Plant Health Institute of Montpellier, France) for valuable discussions and support throughout the project. We also thank Laura Mathieu (Plant Health Institute of Montpellier, France) for her support with the analysis of the split-luciferase data and Vincent Chochois (CIRAD, France) for his assistance with sequence analysis related to the Y2H cDNA library screen.

This work benefited from access to the NMR and RX facilities of the Integrated Biophysics and Structural Biology Platform (PIBBS) of the CBS. PIBBS is a GIS-IBISA platform and belongs to the French Infrastructure for Integrated Structural Biology (FRISBI), supported by the National Research Agency (ANR-10-INBS-05).

We acknowledge the European Synchrotron Radiation Facility (ESRF) for provision of synchrotron radiation facilities. We would like to thank the staff of the ESRF and EMBL Grenoble for assistance and support in using beamline ID30-A1 under proposal number mx-2409. This work was funded by the HORIZON EUROPE European Research Council grant ERC-2019-STG-852482-ii-MAX awarded to Stella Cesari.

Author contributions

Josephine H.R. Maidment: Conceptualization; Data curation; Formal analysis; Investigation; Methodology; Project administration; Resources; Supervision; Validation; Visualization; Writing – original draft; Writing – review & editing. **Svenja C. Saile**: Conceptualization; Data curation; Formal analysis; Investigation; Methodology; Project administration; Resources; Supervision; Validation; Visualization; Writing – original draft; Writing – review & editing. **Aurélien Bocquet**: Investigation; Methodology; Resources; Validation; Writing – review & editing. **Céline Thivolle**: Investigation; Methodology; Resources; Validation; Writing – review & editing. **Léo Bourcet**: Investigation; Methodology; Resources; Validation; Writing – review & editing. **Lisa-Fatimatou Planel**: Investigation; Methodology; Resources; Validation; Writing – review & editing. **Muriel Gelin**: Methodology; Resources; Writing – review & editing. **Thomas Kroj**: Conceptualization; Writing – review & editing. **André Padilla**: Conceptualization; Methodology; Writing – review & editing. **Karine de Guillen**: Conceptualization; Data curation; Formal analysis; Investigation; Methodology; Project administration; Resources; Supervision; Validation; Visualization; Writing – original draft; Writing – review & editing. **Stella Cesari**: Conceptualization; Data curation; Formal analysis; Funding acquisition; Investigation; Methodology; Project administration; Resources; Supervision; Validation; Visualization; Writing – original draft; Writing – review & editing.

Competing interests

The authors declare that they have no conflicts of interest with the contents of this article.